FAR-INFRARED ABSORPTION BY LIQUID NITROGEN AND LIQUID OXYGEN

by

EDWARD H. WISHNOW

B.A., Reed College, 1980

A THESIS SUBMITTED IN PARTIAL FULFILMENT OF

THE REQUIREMENTS FOR THE DEGREE OF

MASTER OF SCIENCE

in

THE FACULTY OF GRADUATE STUDIES

Department Of Physics

We accept this thesis as conforming

to the required standard

THE UNIVERSITY OF BRITISH COLUMBIA

October 1985

In presenting this thesis in partial fulfilment of the requirements for an advanced degree at the University of British Columbia, I agree that the Library shall make it freely available for reference and study. I further agree that permission for extensive copying of this thesis for scholarly purposes may be granted by the Head of my Department or by his or her representatives. It is understood that copying or publication of this thesis for financial gain shall not be allowed without my written permission.

Department of Physics

The University of British Columbia
2075 Wesbrook Place
Vancouver, Canada
V6T 1W5

Date: October 15, 1985

Abstract

This thesis examines the collision induced, far-infrared absorption of homonuclear diatomic molecules. These molecular processes are relevant in the astrophysical environments of planetary atmospheres and galactic molecular clouds, and a brief survey of far-infrared measurements of these regions is presented. The theory of collision induced absorption by molecular rotational transitions is reviewed and a calculation is made of the quadrupolar induced, single rotational transition absorption line intensities of the nitrogen and oxygen molecules. The far-infrared absorption spectra of liquid nitrogen and liquid oxygen at 77K, over the frequency range 5 to 70 cm^{-1}, have been measured. The far-infrared spectrum of liquid oxygen has not previously been reported. The present work includes the design of a low temperature, multiple pass, far-infrared absorption cell intended for low temperature, low density gas measurements. The effect of diffraction on the cell's maximum attainable optical path length, and a model used to estimate the anticipated liquid helium consumption are discussed.

Table of Contents

List of Tables

List of Figures

Acknowledgement

I would like to thank my family and friends for their encouragement of my studies. Among them, Ira Blevis and especially Carolyn Coons have been very supportive, particularly during my early years of graduate school, and I sincerely thank them. I am very thankful of the generous understanding which Anna Fritz has shown towards me over the course of this work.

The members and associates of our laboratory deserve recognition and my thanks for their contributions to this work. Irving Ozier has contributed his support and suggestions to the design of the low temperature cell, as has Sucha Parmar. Vittorio DeCosmo's comments and company have been much appreciated. Alex Leung has made very impressive, not to mention invaluable, design contributions to the low temperature cell. I have learned a great deal of physics from Mark Halpern and I thank him for this and for his help throughout this work. Finally, I would like to thank Prof. Herbert Gush for his confidence in me, and his support, and for including me in his challenging research work, for which I feel very fortunate.

I would like to dedicate this work to my mom and dad.

I. INTRODUCTION

The universe is composed primarily of hydrogen and in our galaxy a large portion of it exists in cold, sparse molecular clouds. Since the molecules within these gas clouds are cold, only the low energy rotational or translational molecular states are highly populated. Molecular transitions between these states correspond in energy to the far-infrared frequency region of electromagnetic radiation. Isolated molecules like hydrogen absorb infrared radiation very weakly because of their symmetry, yet aggregates of these molecules, via collisions or clustering, can absorb more strongly. Other diatomic molecules, in particular nitrogen and oxygen, also absorb radiation by these mechanisms, where nitrogen has an importance in astrophysics due to its prevalence in planetary atmospheres. The motivation for the present work is to gain an understanding of the absorption of far-infrared radiation by homonuclear diatomic molecules. Several aspects of collision induced absorption by these molecules have been investigated: the theory, the absorption of far-infrared radiation by liquid nitrogen and liquid oxygen, and the design of a low temperature optical absorption cell. The first part of this chapter introduces the topics of collision induced absorption and dimer absorption by homonuclear diatomic molecules. The second part reviews the astrophysical measurements to which these spectroscopic results may be applied.

1.1 Molecules And Radiation

When radiation is absorbed by any system, the frequency is related to the energy change of the system by Bohr's frequency condition:

$$E_f - E_i = h\nu = hc\sigma$$

Here, E_i and E_f are the initial and final energy states, h is Planck's constant, ν is the frequency, c is the speed of light, and σ is the frequency in wave numbers, where $\sigma = 1/\lambda$ (in cm^{-1}), and λ is the wavelength. Spectroscopy therefore indicates the nature of optically active energy transitions within matter. In the case of molecules, the types of transitions that may be examined are: (generally decreasing in energy) Electronic, vibrational, and rotational.

The absorption of infrared radiation at frequencies associated with vibrational or rotational transitions, by isolated homonuclear diatomic molecules, is however quite weak. This is a consequence of the symmetry of the ground state of these molecules, whereby they do not possess a permanent electric dipole moment, or its derivatives. Absorption of radiation by this species of molecules occurs only as a result of quadrupole or higher order multipole moments, and is much weaker than that of a molecule with a strong dipole moment, such as HCl.

However, when two or more molecules collide, their

charge distributions may be distorted such that a (transient) dipole moment arises. Since the magnitude and direction of this dipole moment depends on the colliding molecules' internuclear separation, and orientations, the vibrational and rotational transitions of the molecules become infrared active. The dipole moment also depends on the intermolecular distance, and therefore transitions between translational energy states can absorb radiation. Collision induced absorption may be observed in dense systems where collisions are frequent such as the compressed gas or the liquid phase.

The spectrum due to collision induced absorption is different than that of either a normal dipole or quadrupole spectrum. The reason is that the dipole moment induced by collision is of brief duration, say Δt (on the order of 10^{-12} seconds), and due to the uncertainty principle $\Delta E \Delta t \geq \hbar$, the width of the energy states involved, ΔE, is large. In the case of oxygen and nitrogen, this energy spread exceeds the spacing between lines in the rotational spectrum and thus the absorption spectrum of both vibrational and rotational bands is devoid of structure. The shape of the collision induced spectrum resembles the envelope of the normal dipole absorption line spectrum. In the case of hydrogen, where the spacing between the rotational energy levels is wide, the collision induced absorption spectrum shows broad but distinct rotational transitions. A considerable body of literature now exists on the topic of collision induced absorption both of an experimental and theoretical nature.

At certain intermolecular distances, the force between two molecules is attractive and they may be bound together to form a dimer, or Van der Waals molecule. The dimer can possess an electric dipole moment, just as a colliding pair does, with the distinction that it is "permanent" provided the dimer is not dissociated. The hydrogen dimer spectrum has relatively sharp absorption lines at the vibrational and rotational frequencies of the individual molecules, accompanied by satellite lines due to the energy level structure of the dimer itself. The dissociation energy of dimers is low, roughly equal to the depth of the intermolecular potential: for $(H_2)_2$ it is 2.5 cm^{-1}, for $(O_2)_2$ it is 87 cm^{-1} (1). Dimers have a long lifetime only at low temperatures and low densities where the kinetic energy of the molecules is low and collisions are infrequent. Dimer absorption has been observed in the laboratory in the fundamental rotation-vibration band of hydrogen (2)(3) at low temperatures (~20K), and low densities (~2 Amagat), and recently $(H_2)_2$ features have been identified in the H_2 rotational band of the far-infrared spectra of Jupiter and Saturn (4)(5).

In this thesis preliminary measurements are reported of the far-infrared absorption spectrum of liquid nitrogen and liquid oxygen. These measurements have been made over the frequency range 5 to 70 cm^{-1} using a Fourier transform spectrometer designed to measure the spectrum of the submillimeter cosmic background radiation. Although liquid

nitrogen has already been studied, there are not in fact good measurements of the absorption coefficient, particularly at low frequencies. The far-infrared absorption spectrum of liquid oxygen has not been previously been reported.

A review of the theory of collision induced absorption, and a calculation of the expected absorption intensities of oxygen and nitrogen by quadrupolar induced dipole moments are presented in Chapter II. The experimental procedures and results are described in Chapter III.

The original intent of this work was to examine the far-infrared spectrum of low temperature, low pressure, hydrogen gas over the frequency range 20 - 200 cm for the presence of dimers. In order to do this a low temperature multiple pass optical absorption cell was designed. This cell proved to be quite complex and construction has only now started. The cell design is presented in Chapter IV.

1.2 Astrophysical Applications Of Molecular Spectroscopy

The remainder of this chapter is a survey of areas in astrophysics where absorption of radiation by homonuclear diatomic molecules via collision induced dipole moments or dimers is an important physical mechanism. Both these mechanisms as exhibited by hydrogen, nitrogen and rare gas mixtures, are particularly relevant to the study of infrared spectra of the outer planets and their satellites which have atmospheres. These moons are not massive enough to retain

hydrogen, so their atmospheres are composed primarily of nitrogen and methane, and interpretation of their infrared spectra involves collision induced absorption by gaseous and liquid nitrogen. A brief discussion of work in these areas follows.

Hydrogen is the dominant constituent element of the planets Jupiter, Saturn, Uranus, and Neptune, and collision induced absorption has been observed in the mid-infrared spectra of Uranus and Jupiter (6). The far-infrared spectrum of Jupiter (7) shows discrete absorption lines due to rotational transitions of ammonia from 100 - 250 cm^{-1} and then a broad absorption from 300 - 450 cm^{-1} due to collision induced absorption centred on the $S_0(0)$ hydrogen line at 354 cm^{-1}. The assumption underlying the far-infrared results is that the planet is acting as a blackbody source at T_{eff} = 125K, and the absorbing gas lies in an atmospheric temperature inversion layer above the planet. These planetary spectra, in conjunction with laboratory measurements of collision induced absorption by gases, yield information about the composition, pressure, and temperature of the planet's atmospheres.

The recent Voyager interplanetary probes have measured infrared spectra over the range 180 - 1800 cm^{-1}, of Jupiter, Saturn, and their moons at very close range, free of the strong infrared absorption of the earth's atmosphere (8)(9)(10)(11). These spectra show discrete rotational lines of ammonia (180-250 cm^{-1}), vibrational lines of methane (1100-

1300 cm^{-1}), and a broad collision induced absorption band of hydrogen from 300 - 700 cm^{-1}. Hydrogen dimers have been identified in the spectra of Jupiter and Saturn at the $S_0(0)$ line at 354 cm^{-1} and at the $S_0(1)$ line at 587 cm^{-1}. The low temperatures, low pressures and very long path lengths present in these planet's atmospheres provide an ideal environment for the observation of dimer absorption.

Another region of space in which dimers might be expected to form is within molecular clouds in our galaxy. Here the density is low, the temperature is 20 - 60K, and hydrogen dimers can be expected to have a long lifetime. Although the density of a molecular cloud is quite low, an optical path length through it can be extremely long. Radiation passing through such a cloud might be absorbed by dimers, but this remains unobserved. It has been suggested that a submillimeter measurement of the cosmic background radiation spectrum in the direction of a molecular cloud might be distorted by dimer or collision induced effects.

Saturn's moon Titan (surface temperature ~95K) is well known as a satellite with an atmosphere. The Voyager space probe has also taken far-infrared spectra of Titan and interpretation of these spectra has led to the following picture of Titan's atmosphere. The primary atmospheric constituent is nitrogen with methane perhaps playing the role of water in our atmosphere, that is, methane forms clouds in the troposphere, precipitates, and may form liquids or ice on the surface (12). There is an atmospheric cold trap (~70K)

in the troposphere in which condensed nitrogen droplets might be found. Computer models require such droplets of nitrogen or methane to account for the measured spectrum, as collision induced absorption alone is not sufficient (13).

Neptune's moon Triton (surface temperature ~73K) may also have an atmosphere, since methane absorption lines have been detected in its near-infrared spectrum (14). In addition, a strong absorption feature has been detected at 4628 cm^{-1}, exactly at the maximum of the nitrogen first overtone band (15). To produce such a strong feature, the nitrogen must be dense and given Triton's low temperature, it is suggested that Triton may be covered with an ocean of liquid nitrogen. It is unfortunate that the frequency range of the present liquid N_2 spectrum (5 - 70 cm^{-1}) does not overlap with the Voyager spectrometer (180 - 1800 cm^{-1}), as on August 24, 1989, it will pass within 10,000 km of Triton and may record the far-infrared collision induced spectrum of liquid nitrogen. In any case, it will be exciting to see if the present investigations will be applicable to the Voyager results.

The following section presents an outline of the rest of this work. Chapter II discusses in detail the theory of collision induced absorption and a calculation is made of the absorption intensities due to quadrupolar induced dipole moments in nitrogen and oxygen. Chapter III describes the experimental apparatus, a far-infrared Fourier transform spectrometer, with particular attention to special features

of the interferometer and the data analysis. Reported here are new observations of the far-infrared absorption of liquid nitrogen and liquid oxygen, where the far-infrared oxygen spectrum has not previously been published. Finally, Chapter IV discusses the design of a low temperature multiple pass absorption cell intended for far-infrared observations of hydrogen dimers.

II. THE THEORY OF COLLISION INDUCED ABSORPTION

2.1 Review Of The Theory

The following is a review of the theory of collision induced absorption in a gas. It is taken primarily from Van Kranendonk and Kiss (16), and also from references (17)(18)(19). Elements of the theory which are pertinent to liquids are emphasized, but an analysis of collision induced absorption in liquids per se does not currently exist. This discussion concludes with a description of the calculation of the relative strengths of unbroadened rotational absorption lines of nitrogen and oxygen. Later in Chapter III, these calculated line intensities are compared to the experimental results.

Starting from an experimental perspective, the absorption coefficient measured is $A(\sigma)$ which is defined as:

$$A(\sigma) = \frac{1}{l} \ln \frac{I_B(\sigma)}{I_S(\sigma)} \quad , \tag{2.1}$$

where σ is the frequency, in cm^{-1}, l is the length of the sample cell, $I_B(\sigma)$ is the background spectrum, and $I_S(\sigma)$ is the sample spectrum. The integrated absorption coefficient α is:

$$\alpha = \int A(\sigma)\, d\sigma \quad , \tag{2.2}$$

where this integral is taken over the entire absorption band. The integrated absorption coefficient per wavelength $\tilde{\alpha}$ is:

$$\tilde{\alpha} = \int \tilde{A}(\sigma)\, d\sigma = \int \frac{1}{\sigma} A(\sigma)\, d\sigma \quad , \tag{2.3}$$

where $\tilde{A}(\sigma)$ is the absorption coefficient per wavelength, $\tilde{A}(\sigma) = \lambda A(\sigma)$. The integrated absorption coefficient per wavelength is also called the integrated intensity.

The absorption coefficient associated with a specific dipole transition is given by: (19)

$$A_{if}(\sigma) = \frac{4\pi^2}{3\hbar c V} \sigma \sum_{if} (P_i - P_f) |\vec{\mu}_{if}|^2 \delta(\sigma - \sigma_{if}) . \quad (2.4)$$

Here σ is the frequency, V is the volume, P_i and P_f the Boltzmann factors (discussed later) for the initial and final states, $\vec{\mu}$ is the matrix element of the dipole moment of the system between the states i and f, and $\sigma_{if} = (E_f - E_i)/hc$ where E_i and E_f are the energies of the initial and final states respectively.

The integrated intensity in the gas for a specific rotational transition is:

$$\tilde{\alpha}(r,r') = \frac{C}{V} \sum_{t<t'} (P_r P_t - P_{r'} P_{t'}) |\langle r't'|\vec{\mu}|rt\rangle|^2$$

where $C = 4\pi^2/3hc$, and r and r' are the initial and final rotational states, t and t' are the initial and final translational states, P is the Boltzmann factor, and $\vec{\mu}$ is the dipole moment which is a function of the molecule's orientations and positions. The summation takes place over pairs of states for which $E_r + E_t < E_{r'} + E_{t'}$, and if the rotational line $r \rightarrow r'$ is greater than zero frequency, this sum can be extended over all states t,t'. The translational aspect of the intensity is taken into account by considering

rotational transitions in a fixed configuration of molecules, and then averaging over all configurations, by the inclusion of a configurational distribution function.

The collision induced integrated intensity can be written in powers of the density n = N/V , where N is the number of molecules and V is the volume.

$$\tilde{\alpha} = \tilde{\alpha}_1 n^2 + \tilde{\alpha}_2 n^3 + \ldots$$

$\tilde{\alpha}_1$ is the binary absorption coefficient, $\tilde{\alpha}_2$ is the ternary absorption coefficient etc. For low density gases, only binary collisions need to be considered, however for liquids, interactions are probably taking place between many molecules and this assumption is not correct.

The binary absorption coefficient for a specific rotational line B is then:

$$\tilde{\alpha}_1(B) = \frac{1}{2} C (Pr - Pr') \int |\vec{M}_{rr'}(\vec{R})|^2 g_0(\vec{R}) \, d\vec{R} \qquad (2.5)$$

The expectation value of the total dipole moment in eqn. (2.5) is now written as an integral over the matrix elements of the pair dipole moment times the pair distribution function.

$$\vec{M}_{rr'}(\vec{R}) = \langle r' | \vec{\mu}(\vec{\omega}_1, \vec{\omega}_2, \vec{R}) | r \rangle \qquad (2.6)$$

is the matrix element of the pair dipole moment which is a function of the molecules orientations $\vec{\omega}_1$, $\vec{\omega}_2$ and separation $\vec{R}$. $g_0(\vec{R})$ is the low density pair distribution

function of the molecules. At high temperatures it is equal to: $\exp(-V(R/d)/kT)$, where $V(R/d)$ is the intermolecular potential, for instance the Lennard-Jones potential, where d here is the Lennard-Jones molecular diameter.

Now examine the matrix element of the dipole moment $\hat{M}_{rr'}(\vec{R})$. The situation is depicted in the following drawing.

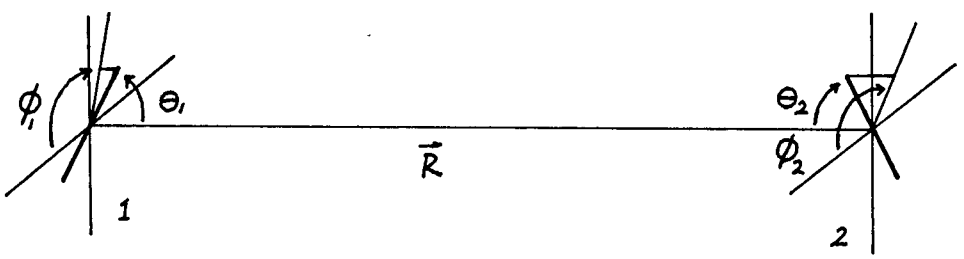

The induced dipole of the pair is a function of their distance apart and their relative orientations to an axis between their centres of mass, where $\vec{\omega}_1 = (\theta_1, \phi_1)$, and $\vec{\omega}_2 = (\theta_2, \phi_2)$. The pair dipole moment $\vec{\mu}(\vec{\omega}_1, \vec{\omega}_2, \vec{R})$ can be written in terms of the spherical harmonics.

$$\mu_K(\vec{\omega}_1, \vec{\omega}_2, \vec{R}) = 4\pi \sum_{\lambda_1 \mu_1 \lambda_2 \mu_2} D_K(\lambda_1 \mu_1 \lambda_2 \mu_2)\, Y_{\lambda_1}^{\mu_1}(\vec{\omega}_1)\, Y_{\lambda_2}^{\mu_2}(\vec{\omega}_2)$$

$K = 0, \pm 1$ refers to components of $\vec{\mu}$ in a spherical coordinate system where 0 corresponds to the z axis which lies along $\vec{R}$, ± 1 refer to bases corresponding to the directions $\mp \frac{1}{\sqrt{2}}(X \pm iY)$. The $D_K(\lambda_1 \mu_1 \lambda_2 \mu_2)$ are the coefficients of the dipole moment in the basis of the spherical harmonics.

The rotational part of the wavefunction of a two molecule system is:

$$\psi_r = Y_{J_1}^{m_1}(\vec{\omega}_1)\, Y_{J_2}^{m_2}(\vec{\omega}_2) \quad \text{thus} \quad |r\rangle = |J_1 m_1 J_2 m_2\rangle$$

in eqn. (2.6), $J_1 m_1$, $J_2 m_2$ refer to the angular momentum and the projection of of the angular momentum perpendicular to $\vec{R}$ for molecules 1 and 2. Eqn. (2.6) for the dipole moment matrix elements is now:

$$\vec{M}_{rr'}(\vec{R}) = \langle J_1' m_1' J_2' m_2' | \mu_K(\vec{\omega}_1, \vec{\omega}_2, \vec{R}) | J_1 m_1 J_2 m_2 \rangle$$

Integrating over the initial and final states of angular momentum using the expansion of $\vec{\mu}$ into spherical harmonics yields the dipole moment matrix elements. From this integration and the properties of the spherical harmonics, the selection rules for the allowed angular momentum transitions are obtained. These selection rules yield non-zero dipole matrix elements only when λ_1 and λ_2 have the values: 0, 2, 4, ..., with the restriction that λ_1 and λ_2 cannot simultaneously equal zero. Allowed rotational transitions are therefore from $J \rightarrow J+2$, $J+4, \ldots,$. Using these dipole matrix elements, and only taking the expansion in the spherical harmonics to the λ_1, $\lambda_2 = 2$ terms, the binary absorption coefficient is obtained from eqn. (2.5)

The binary absorption coefficient $\tilde{\alpha}_1(B)$ is a sum of single rotational transitions and double rotational transitions. Single transitions are when one molecule of the colliding pair goes from $J \rightarrow J+2$ and the other makes no transition. Double transitions are when both molecules make transitions: $J_1 \rightarrow J_1+2$, $J_2 \rightarrow J_2+2$. For single transitions the

binary absorption coefficient is:

$$\tilde{\alpha}_1(J) = C\, L(J) \left[I_0(20) + L' I_0(22) \right] \qquad (2.8)$$

The J dependent functions L(J) and L' arise from the integration over the wavefunctions and the dipole moment in the spherical basis.

$$L(J) = L_2(J, J+2) \left[P(J) - P(J+2) \right]$$

$$L' = \sum_{J=0}^{\infty} L_2(J,J)\, P(J)$$

where $L_2(J,J+2) = \dfrac{3(J+1)(J+2)}{2(2J+3)}$ & $L_2(J,J) = \dfrac{J(J+1)(2J+1)}{(2J-1)(2J+3)}$

$I_0(\lambda_1, \lambda_2)$ is the remaining integral over the radial dependence of the coefficients of the dipole moment and the pair distribution function.

$$I_0(\lambda_1, \lambda_2) = \int \sum_{K \mu_1 \mu_2} | D_K(\lambda_1 \mu_1, \lambda_2 \mu_2) |^2 g_0(R)\, dR$$

where λ_1, λ_2 are 0 or 2. The binary absorption coefficient for double transitions is:

$$\tilde{\alpha}_1(J_1, J_2) = C \left[1 - \tfrac{1}{2} \delta(J_1, J_2) \right] L(J_1, J_2)\, I_0(22) \qquad (2.9)$$

where

$$L(J_1, J_2) = L_2(J_1, J_1+2)\, L_2(J_2, J_2+2) \times$$
$$\left[P(J_1) P(J_2) - P(J_1+2) P(J_2+2) \right]$$

The dipole moment coefficients $D_K(\lambda_1 \mu_1, \lambda_2 \mu_2)$ are obtained from the dipole induced in one molecule due to the quadrupolar field of the other molecule acting upon the

polarizability of the first molecule. The following is an aside which discusses the phenomenological basis for these coefficients.

The dipole moment $\vec{\mu}$ in a polarizable dielectric medium is obtained from:

$$\vec{\mu} = \alpha \cdot \vec{E} \qquad (\mu_i = \alpha_{ij} E^j)$$

where α is the polarizability tensor and $\vec{E}$ the electric field. The electric field at a point in space is given by:

$$\vec{E} = -\nabla V$$

The potential at molecule 2 due to the charge distribution of molecule 1 which is at a distance R can be written as a multipole expansion: (20)

$$V(2) = \sum_{n=0}^{\infty} \frac{1}{R^{n+1}} \int r^n P_n(\cos\theta)\, \rho\, d\tau$$

The drawing below explains the physical situation.

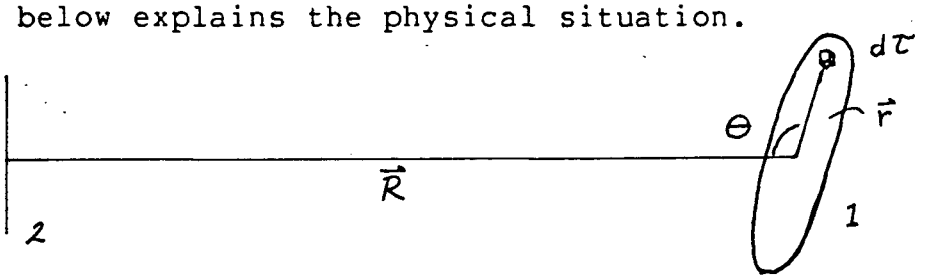

$\vec{R}$ is the distance between the molecules, ρ is the charge density of molecule 1, $\vec{r}$ is the distance from an origin at the centre of mass of molecule 1 to a volume element $d\tau$, θ is the angle between $\vec{R}$ and $\vec{r}$, and P_n are the Legendre polynomials. The integral is over the volume of molecule 1.

As previously stated there is no dipole associated with homonuclear diatomic molecules, so the first significant term is this expansion is the quadrupolar term,

$$V(2) = \frac{1}{R^3}\int r^2 P_2(\cos\theta)\rho\, d\tau = \frac{1}{R^3}\int r^2\left(\frac{3}{2}\cos^2\theta - \frac{1}{2}\right)\rho\, d\tau$$

For discrete charges, the quadrupole moment becomes an expectation value. (19)

$$Q = \left\langle \sum_i e_i\, r_i^2\, P_2(\cos\theta_i)\right\rangle$$

where e_i, r_i, θ_i, are the magnitude, and polar coordinates of the ith charge from an origin at the centre of mass of molecule 1.

The magnitude of the electric field at molecule 2 due to the quadrupolar potential of molecule 1 is:

$$|\vec{E}(2)| \propto \frac{1}{R^4} Q$$

The magnitude of the induced dipole moment of molecule 2 is then:

$$|\vec{\mu}| \propto \frac{\alpha Q}{R^4}$$

where α is the average polarizability $\alpha = \frac{1}{3}(2\alpha_\perp + \alpha_\parallel)$. Since the polarizability is a tensor, the dipole moment also depends on the anisotropy of the polarizability δ. If the quadrupolar field of each molecule of the pair induces a dipole in the other, the net dipole moment of the pair is $\vec{\mu} = \vec{\mu}_1 + \vec{\mu}_2$. Since the electric field of a quadrupole

rotates twice as fast as the molecule, the induced dipole moment will oscillate at twice the rotational frequency. This demonstrates heuristically, the selection rules that light will be absorbed by dipole moment transitions of $\Delta J = 2$.

The coefficients D_K are given by VanKranendonk and Kiss as:

$$D_0(2000) = \frac{3}{\sqrt{15}} \frac{\alpha Q}{R^4} \qquad D_1(2100) = \frac{-3}{\sqrt{15}} \frac{\alpha Q}{R^4}$$

$$D_1(2120) = \frac{-4\sqrt{3}}{15} \frac{\gamma Q}{R^4} \qquad D_1(222-1) = \frac{\sqrt{2}}{15} \frac{\gamma Q}{R^4}$$

and 10 other coefficients from the symmetry properties of the D_K coefficients. The $1/R^4$, α , and Q dependence of the dipole moment matrix elements is clear. γ is the anisotropy of the polarizability of the molecule, $\gamma = \alpha_{\parallel} - \alpha_{\perp}$. Inserting these coefficients into eqns. (2.8) and (2.9) yields binary absorption coefficients.

This discussion only covers the dipole moment induced by the long range quadrupolar interaction. This is the dominant interaction for rotational transitions of the molecules, but this is not the case for the translational band, where the isotropic overlap interaction induced dipole moments are important (19). To include short range overlap interactions, the electronic part of the wave function must be included in the calculation of the dipole moment matrix elements. The

coefficients D_K obtained via this calculation have an exp(-R) dependence. A complete account of the collision induced absorption adds these coefficients to the quadrupolar coefficients in the calculation of the radial dependent integral $I_0(\lambda_1 \lambda_2)$.

2.2 Calculation Of Absorption Intensities

To compare the measured absorption coefficients to the collision induced absorption theory a calculation was made of the unbroadened rotational absorption lines (stick spectrum) based on eqns. (2.8) and (2.9). The pair distribution function $g_0(\vec{R})$ is not known for the liquid case so the radial dependent integrals were not evaluated in this calculation. The absolute intensities of absorption from this calculation are therefore not known, but the relative strength of absorption is proportional to the J dependence of the binary absorption coefficient.

Equations (2.8) and (2.9) can be simplified considerably if absolute intensities are not required. In particular the radial dependence of the binary absorption coefficient is considered a constant. The simplified form of the binary absorption coefficient in terms of J for single transitions is:

$$\tilde{\alpha}_1(J) \propto L(J)\left[(\alpha Q)^2 + L' \frac{88}{225}(\gamma Q)^2\right] \qquad (2.10)$$

where α is the average polarizability, Q is the quadrupole

moment, γ is the anisotropy of the polarizability and L(J) and L' are defined previously. The simplified form of the binary absorption coefficient for double transitions is:

$$\tilde{\alpha}_1(J_1,J_2) \propto \left[1 - \frac{1}{2}\delta(J_1,J_2)\right] L(J_1,J_2) \frac{88}{225} (\gamma Q)^2 \quad (2.11)$$

where $L(J_1,J_2)$ is given above. Note that the double transitions depend on only the anisotropy of the polarizability. For nitrogen, the single transition coefficients are about 1000 times larger than the double transitions coefficients for a temperature of 77K and frequencies below about 60 cm^{-1}.

The constants which are important for the calculation are tabulated below:

	Q	α	γ
N_2	1.46×10^{-26} esu (21)	1.74×10^{-24} cm^3 (21)	0.696×10^{-24} cm^3 (21)
O_2	0.4×10^{-26} esu (22)	1.59×10^{-24} cm^3 (23)	1.1×10^{-24} cm^3 (23)

Table 1 - Quadrupole moment, polarizability, and anisotropy of the polarizability for the nitrogen and oxygen molecules

Absorption line intensities can be obtained from the binary absorption coefficients for comparison to the measured absorption coefficients. To obtain a relative absorption intensity, for a specific rotational line, the binary absorption coefficients are multiplied by the frequency

associated with the rotational transition.

$$A_{\sigma}(J)_{\text{calculated}} \propto \sigma(J)\,\tilde{\alpha}_1(J) + \sigma(J_1,J_2)\,\tilde{\alpha}_1(J_1,J_2) \quad (2.12)$$

where $\sigma(J)$ are the frequencies of single transitions and $\sigma(J_1,J_2)$ are the frequencies of double transitions. To complete the calculation of the stick spectrum, the frequencies of the various transitions must be obtained.

The energy states of a diatomic vibrating-rotator are described by a rotational constant B, and a centrifugal distortion constant D. B is inversely proportional to the moment of inertia of the molecule. The energy spectrum of a rigid rotator is obtained by multiplying the eigenvalues of the angular momentum squared, J(J+1) by B. The spectrum of the vibrating-rotator deviates from the rigid rotator spectrum because of the centrifugal distortion of the molecule and the additional feature that the internuclear separation is not fixed but is described by a probability distribution. The indeterminancy of the internuclear distance is referred to as the "zero point" energy of the molecule. Both B and D are modified by the vibrational state of the molecule. This is because the internuclear separation is changing and therefore so is the moment of inertia and centrifugal distortion of the molecule.

The "rotational terms" of the vibrating-rotator in the vibrational ground state are: (24)

$$F(J) = \frac{E_r}{hc} = B_0 J(J+1) - D_0 J^2(J+1)^2 \quad (2.13)$$

B_o is the rotational constant in the vibrational ground state. To first approximation,

$$B_o = B_e - \alpha_e (v + \tfrac{1}{2}) \text{ , where } v = 0.$$

B_e is the rotational constant of the molecule corresponding to the equilibrium internuclear distance r_e. $B_e = h/8\pi^2 c I_e$, where I_e is the equilibrium moment of inertia. α_e is a constant representing the change in internuclear separation. D_o is the centrifugal distortion constant in the vibrational ground state.

$$D_o = D_e - \beta_e (v + \tfrac{1}{2}) \text{ , where } v = 0.$$

D_e is the equilibrium centrifugal constant, $D_e = 4B_e^3/\omega_e^2$. is given as:

$$\beta_e = D_e \left(\frac{8\omega_e \chi_e}{\omega_e} - \frac{5\alpha_e}{B_e} - \frac{\alpha_e^2 \omega_e}{24 B_e^2} \right)$$

where the constants ω_e, $\omega_e \chi_e$, α_e, and B_e are obtained from tables of spectroscopic molecular constants. These constants for nitrogen and oxygen are tabulated below (25). (all in cm^{-1})

	B	α_e	ω_e	$\omega_e\chi_e$	B_o	D_o
N_2	1.9987	0.01781	2358.07	14.188	1.990	5.743×10^{-6}
O_2	1.44567	0.01579	1580.36	12.073	1.438	4.843×10^{-6}

Table 2 - Rotational constants of the nitrogen and oxygen molecules

The frequency of light absorbed by a rotational transition is given by:

$$\sigma = F(J+2) - F(J) = (4B_o - 6D_o)(J+\tfrac{3}{2}) - 8D_o(J+\tfrac{3}{2})^3 \qquad (2.14)$$

The frequency of a double transition $J_1 \rightarrow J_1+2$, $J_2 \rightarrow J_2+2$, is given by $\sigma = \sigma_1 + \sigma_2$ where σ_1, σ_2 are calculated from the above.

Finally, the Boltzmann factors P(J) in this calculation are given by:

$$P(J) = \frac{S(J)\, e^{-F(J)hc/kT}}{\sum_{J=0}^{\infty} S(J)\, e^{-F(J)hc/kT}} \qquad (2.15)$$

Dividing by the sum of all Boltzmann factors normalizes the temperature dependent population distribution. Here S(J) is the degeneracy of a given rotational state due to the nuclear spin statistics of the molecules, this is discussed below.

One last feature of the stick spectrum is the influence of the nuclear spin on the molecular absorption spectrum. The total wavefunction of a diatomic molecule also involves a

nuclear spin part. For a homonuclear molecule, the total wavefunction is:

$$\Psi_{TOTAL} = \psi_{electronic}\,\psi_{rotational}\,\psi_{nuclear}$$

It must be symmetric with respect to interchange of the nuclei if the nuclei are bosons, and antisymmetric if the nuclei are fermions. There are $(2I + 1)^2$ possible nuclear spin states, $(2I + 1)(I + 1)$ of these states are symmetric and $(2I + 1)I$ are antisymmetric, where I is the spin of the nucleus. The nucleus of nitrogen has 14 particles, the net nuclear spin in the ground state is I = 1. The nucleus of oxygen has 16 particles, the net nuclear spin in the ground state is I = 0. Both nitrogen and oxygen nuclei are bosons.

The electronic ground state of nitrogen is $^1\Sigma_g^+$ this is a symmetric wavefunction (26). The nucleus of nitrogen is a boson which is symmetric and it is required that the total wavefunction be symmetric. Since the even rotational J states are symmetric they combine with the $(2I + 1)(I + 1)$ symmetric nuclear spin states and have a statistical weight of 6. The odd rotational states are antisymmetric and combine with the $(2I + 1)I$ antisymmetric nuclear spin states and have a statistical weight of 3. Therefore for nitrogen, the line intensities calculated above are multiplied by 2 for even rotational transitions.

The electronic ground state of oxygen is $^3\Sigma_g^-$ which has an antisymmetric wavefunction (26). The nucleus of oxygen is a boson which has a symmetric wavefunction. Therefore, to

obtain a symmetric total wavefunction, the antisymmetric nuclear spin states must be combined with the even J rotational states. The symmetric nuclear spin states are then combined with the odd rotational states. The even rotational levels have a statistical weight of $(2I + 1)I$ or zero. The odd rotational levels have a statistical weight of $(2I + 1)(I + 1)$ or 1. Hence, molecular oxygen, in the electronic ground state, only exists in odd rotational energy levels, and the absorption spectrum is limited to frequencies which correspond to odd rotational transitions.

The results of the relative intensities of the quadrupolar induced single transition absorption lines, at a temperature of 77K, are displayed below. These results are also displayed on the plots of the measured absorption coefficients, figs. 7 and 8.

NITROGEN

SINGLE TRANSITIONS:FREQS, LINE INTENSITIES

J	FREQS.	INTENTS.
0	11.9398	0.502182E-01
1	19.8992	0.108585
2	27.8579	0.489118
3	35.8157	0.392025
4	43.7722	1.00000
5	51.7272	0.535227
6	59.6803	0.990866
7	67.6314	0.403938
8	75.5802	0.587287
9	83.5262	0.191948
10	91.4694	0.227040
11	99.4099	0.610225E-01
12	107.346	0.598390E-01
13	115.280	0.134175E-01
14	123.208	0.110314E-01
15	131.133	0.208214E-02
16	139.053	0.144573E-02
17	146.968	0.231081E-03
18	154.878	0.136181E-03
19	162.784	0.185100E-04
20	170.683	0.929140E-05

OXYGEN

SINGLE TRANSITIONS:FREQS, LINE INTENSITIES

J	FREQS.	INTENTS.
1	14.3793	0.140019
3	25.8803	0.580474
5	37.3772	0.984951
7	48.8680	1.00000
9	60.3508	0.692051
11	71.8234	0.346924
13	83.2859	0.130268
15	94.7332	0.373910E-01
17	106.166	0.831551E-02
19	117.581	0.144622E-02

Table 3 - Frequencies and absorption intensities of quadrupolar induced single rotational transitions in nitrogen and oxygen molecules, *at 77K.*

III. EXPERIMENTAL APPARATUS AND RESULTS

The experiments described in this thesis were performed in conjunction with the initial testing of a rocket borne, helium cooled interferometer, designed to measure the subimillimeter cosmic background radiation spectrum (27). These tests demonstrated that the interferometer's optics, scan mechanism, and data collection scheme worked according to design. In addition to confirming the interferometer operation, experiments were undertaken to measure the absorption of room temperature and cold far-infrared optical materials for use as far infra-red detector filters (28). In the course of these experiments, the absorption coefficients of liquid nitrogen and liquid oxygen were also measured. The first part of this chapter describes the experimental apparatus and procedure. The second part discusses the liquid N_2 and O_2 spectra.

3.1 Experimental Apparatus And Procedures

The measurements were obtained using the interferometer mentioned above as a laboratory Fourier transform spectrometer. In general, a Fourier transform spectrometer is an instrument which induces a variable path difference between two optical paths, where the two light beams are then combined at a detector. The signal generated by the detector is called the interferogram and is proportional to the autocorrelation function of the intensity of the

electromagnetic radiation incident on the interferometer. The power spectrum of the incident radiation is obtained from the Fourier transform of the interferogram.

The design of an interferometer depends on what is the most important parameter of the desired spectrum: resolution, spectral bandwidth, absolute intensity, etc. The most important aspects of the cosmic background measurement are intensity calibration and wide spectral range. Hence, the rocket instrument is a polarizing dual input - dual output interferometer, with an area solid angle product of about 0.1 cm^2 steradian.

The advantage of this design is that the signal measured at each detector is proportional to the difference in brightness between the two inputs. In the cosmic background experiment, this permits the spectrum of the sky to be compared directly with that of a blackbody calibrator whose temperature can be set near 2.7K.

The optical path of the polarizing interferometer used in this work is shown in fig. 1. Light from a 600°C blackbody source is collimated by a TPX lens, which projects a quasi-parallel beam into the interferometer. The beam encounters a vertical (out of the picture plane) wire grid polarizer A; approximately half the beam is transmitted 1 (polarized horizontally), and half reflected 2 (polarized vertically). Beam 2 is reflected off mirror B and proceeds to the wire grid beamsplitter C, whose wires are inclined about 45° to the plane of the diagram. For each initial beam

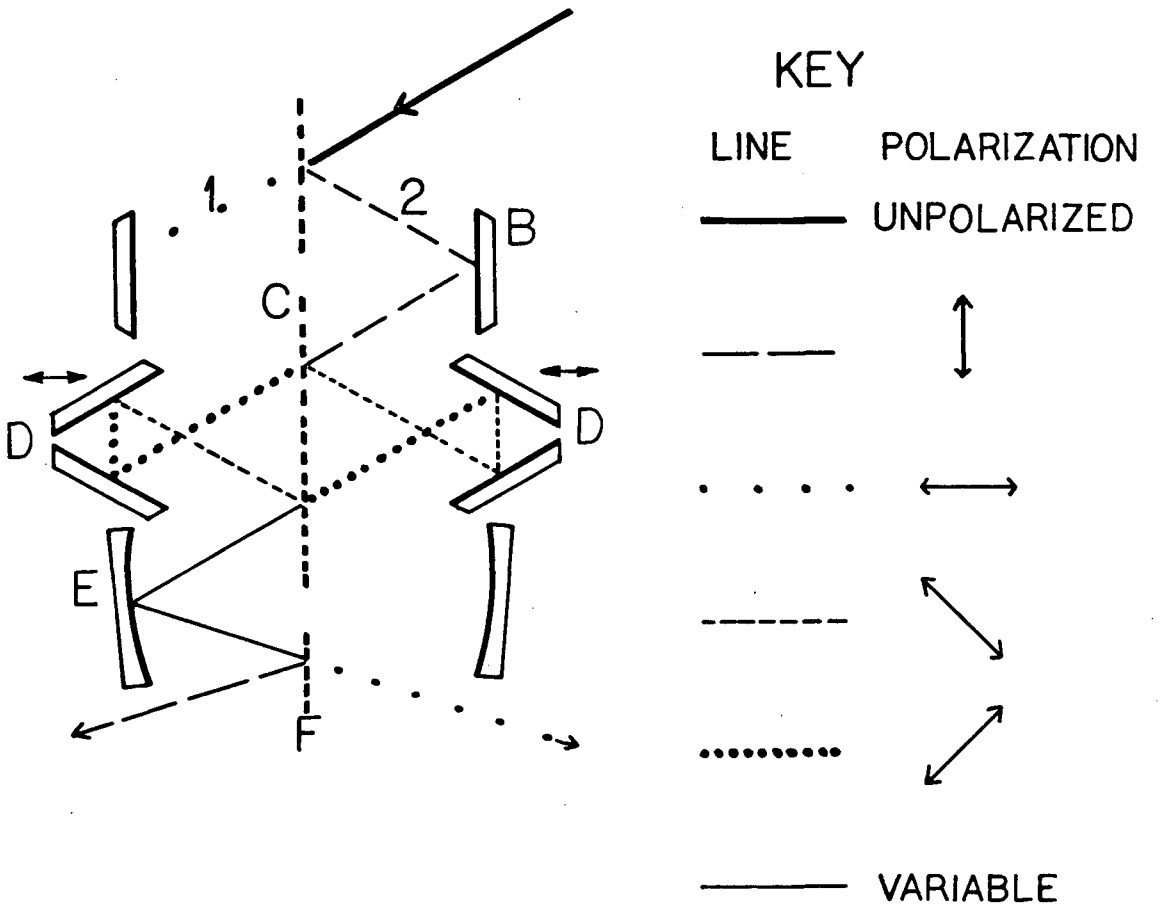

Figure 1 - Interferometer optical path
Text traces light path from blackbody source through system. Optical components are: initial polarizer A, mirror B, polarizing beamsplitter C, scanning mirrors D, mirror E, final polarizer F, and detector.

(1 or 2), half the beam is transmitted and half reflected. The beam now reflects off the twin 60° mirrors D, which may be moved back and forth, indicated by the arrows. The polarization of the beam is rotated 90° with respect to the beamsplitter by reflection off the twin mirrors. A beam which was initially reflected by the beamsplitter is now transmitted, likewise a beam which was initially transmitted by the beamsplitter is now reflected. The combined beams now reflect from mirror E, and then encounter another vertical wire grid, the analyzing polarizer F. Approximately half of the "transmitted-reflected" beam is transmitted through this polarizer and combined with half of the "reflected-transmitted" beam, which is reflected by this polarizer. This beam is now composed of light from two different optical paths of different lengths, due to the position of the moving mirrors. The light beam is unpolarized, it is focussed to a detector and an interferogram is measured. This discussion traces the path of only half the light from a single input. If both inputs are considered, the light at each detector is then a combination of "reflected-transmitted" and "transmitted-reflected" light, from each input.

The beamsplitters were designed and constructed at U.B.C., they are optimized for operation in the frequency range 0 - 200 cm^{-1}. Each beamsplitter consists of 18μm gold plated tungsten wire spaced every 36μm, to form a wire grid.

The resolution of a Fourier transform interferometer is proportional to the maximum path length difference between

the two optical paths. If the interferograms are not apodized before Fourier transforming, the resolution of the spectrum is $\Delta\sigma = \frac{1}{2L}$, where $\Delta\sigma$ is in cm^{-1}, and L is the maximum path length difference in cm. For this interferometer, double sided interferograms of 1024 points were transformed yielding a spectrum of 512 points spanning a frequency range of 0 - 235 cm^{-1}. The frequency scale was calibrated by matching lines in the measured spectra to known water vapor absorption lines. The resolution of the spectra from digital sampling is $0.46\ cm^{-1}$. The following table contains information pertinent to the resolution of this interferometer.

	Expected	Actual
Max. path difference ΔL	1.16 cm	$\frac{1109}{1024} \times \frac{1}{2 \times .459} = 1.18cm$
# samples / scan	1067	1109
ΔL per sample	21.8 μm	21.1 μm
Max. frequency	229 cm^{-1}	235.0 cm^{-1}
Line resolution	0.54 cm^{-1}	0.51 cm^{-1}

Table 4 - Interferometer parameters, as specified in the design and as measured

where the line resolution above is described by the width of

a sinc function at half maximum ($\Delta\sigma=\frac{1}{1.66L}$). This is different from the resolution as described by the first zeros of the sinc function occuring at $\Delta\sigma=\frac{1}{2L}$, as mentioned above.

The detector for the laboratory experiments was a silicon monolithic bolometer brought by Dr. Mark Halpern from MIT (29). This detector consists basically of a 5 mm square ion implanted silicon wafer connected to the liquid helium reservoir by thin thermally resistive legs. In order to absorb radiation it has been coated with a film of bismuth thereby impedance matching the bolometer and free space. Since the detector is poorly coupled to the helium bath its temperature is sensitive to the radiation load on it. The electrical resistance of the bolometer, nominally 1 MΩ at 4.2K, is very temperature dependent and therefore, changes in radiative power can be measured as voltage fluctations, if a constant current ($\sim 10^{-6}$ amp.) is passed through the device. This is done here using a special cooled preamplifier.

The bolometer, bias resistor, preamplifier, and a filter wheel for cold optical filter measurements, are all attached to the cold plate of a modified Infrared Laboratory helium dewar. Light is concentrated on the bolometer by a polyethylene lens followed by a copper condensing cone. Cold optical filters were placed just behind the lens to lessen the change in total power absorbed by the bolometer upon insertion of the sample. These filters define the high frequency cutoff of the experiments. The low frequency

cutoff is 2.4 cm^{-1} and is defined by the exit aperture of the condensing cone.

The optical filters for the May 17, 1985 experiments (hereafter called the low frequency experiments) gave a high frequency cutoff of 40 cm^{-1} (chosen for dielectric filter measurements (28)). These filters were: a polyethylene lens, 1.05 mm thick fluorogold, 0.014" black polyethylene, and a 1.94 to 2.01 mm plexiglass wedge. The optical filters for the May 30 experiments (the high frequency experiments) gave a high frequency cutoff of 80 cm^{-1}. These filters were: a polyethylene lens, 0.005" black polyethylene, 4 sheets of 0.002" mylar, and 1.01 mm NaCl.

The data aquisition scheme for the laboratory is controlled by a PDP Micro-11 computer system. Voltages from the experiment are measured by an analog-digital converter (Analog Devices RT1-1250 12-bit, 32 channel device) controlled from an assembly language program run by the computer. The computer responds to external triggers generated by the moving mirror system, and each interferogram is sampled about 1110 times. For the high frequency experiments, a capacitance gauge mounted directly on the moving mirror carriage measures the mirror displacement. The signal from this gauge is sampled immediately after the detector signal.

Once the experiments are completed and the data has been written to tape, the data analysis is done on the U.B.C. main computer, an Amdahl V8. The interferograms are Fourier

transformed and the resulting spectra are averaged. Procedures used in the Fourier transform process may differ, and it is worthwhile to follow in detail the procedure for this work.

The raw data consists of interferograms of 1110 samples, and there were usually 28 interferograms per data set. The first step in the analysis is to find the 28 maxima of the data set, near the zero path difference of each interferogram. 1024 point interferograms are obtained by selecting 512 points on either side of each maximum. Each interferogram is complex Fourier transformed, resulting in 512 pairs of real (cos) and imaginary (sine) Fourier coefficients. These are used to calculate a modulus and a phase. Fig. 2 below, taken from the analysis of a typical background run, shows the interferogram, and the modulus and the phase angle as a function of frequency.

If the interferogram were perfectly symmetric, and if the maximum sample coincided exactly with the zero path difference, the sine coefficients would be zero and the spectrum would equal simply the cosine transform coefficients. In reality neither of these conditions are fulfilled. Phase shifts introduced by the detector-amplifier combination cause an asymmetry in the interferogram, and the sampling is not exactly synchronized with the zero point of the moving mirror system.

To obtain a spectrum corrected for the sampling error, the cosine coefficients are mapped onto the x axis in a two

dimensional Cartesian system, and the sine coefficients are mapped mapped on the y axis. These axes are orthogonal to the frequency axis. The intensity of the spectrum at a given frequency is a vector $\vec{V}$ in this x-y plane. This is pictured below, where the sampling error is considered to be a "phase angle" ϕ_f that $\vec{V}$ makes with the x axis.

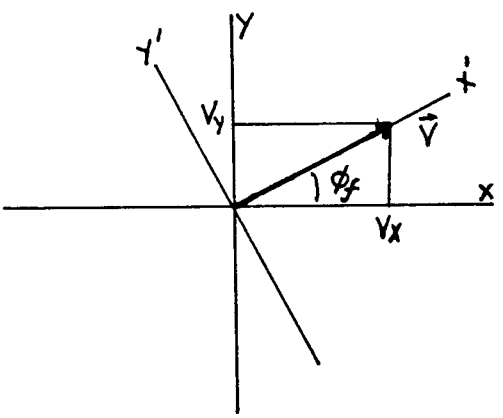

where $\phi_f = \arctan\left(\frac{V_y}{V_x}\right)$, defined over $0 \rightarrow 2\pi$.

To reduce the phase angle to zero, the components of $\vec{V}$ are found in a rotated coordinate system. The components of a vector in a rotated coordinate system are:

$$x' = x \cos\phi + y \sin\phi$$

$$y' = -x \sin\phi + y \cos\phi$$

The new coordinate system is obtained by rotating through the phase angle ϕ_f so that the x' axis lies along the spectral intensity $\vec{V}$. In this new coordinate system $\vec{V}$ has a non-zero component only along the x' axis.

$$V_x' = V_x \cos\phi_f + V_y \sin\phi_f \qquad (3.1)$$

In the computer analysis, the phase angles ϕ_f are fitted with polynomial in the frequency over the spectral range where these coefficients are not fluctuating wildly, that is where there is appreciable intensity. V_x' is found from eqn. (3.1), where ϕ_f is obtained from the polynomial fit to the measured phase. This procedure is equivalent to symmetrizing the interferogram, but is more rapid from a computational point of view, as it does not involve a convolution. Using the actual phase angle ϕ_f would exactly symmetrize the interferogram, but using the fitted phase provides a low resolution phase correction to the interferogram. Fig. 3 shows the polynomial fit to the phase and the spectrum $V_x'(\sigma)$.

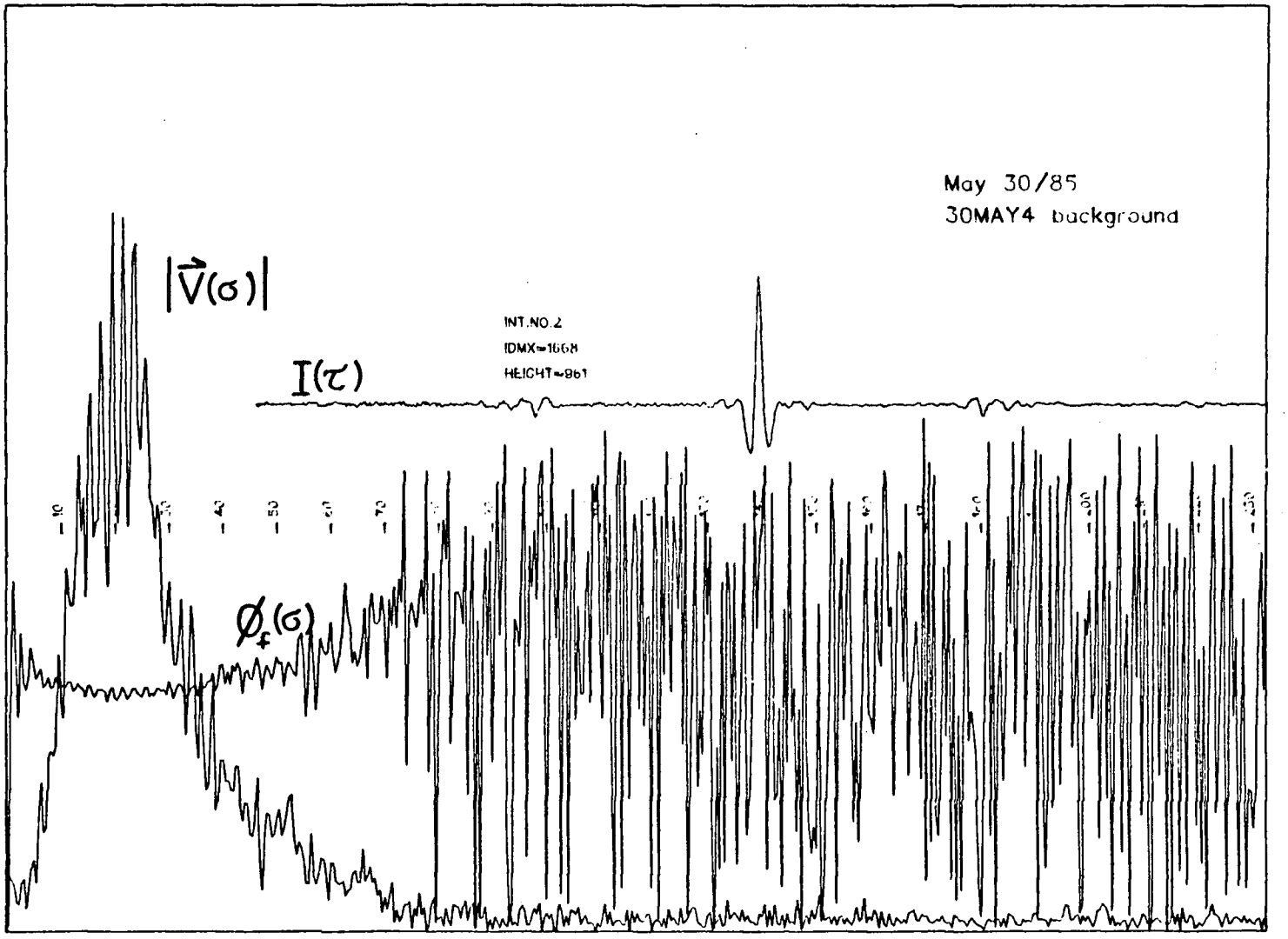

Figure 2 - Interferogram, modulus spectrum and phase angle as a function of frequency

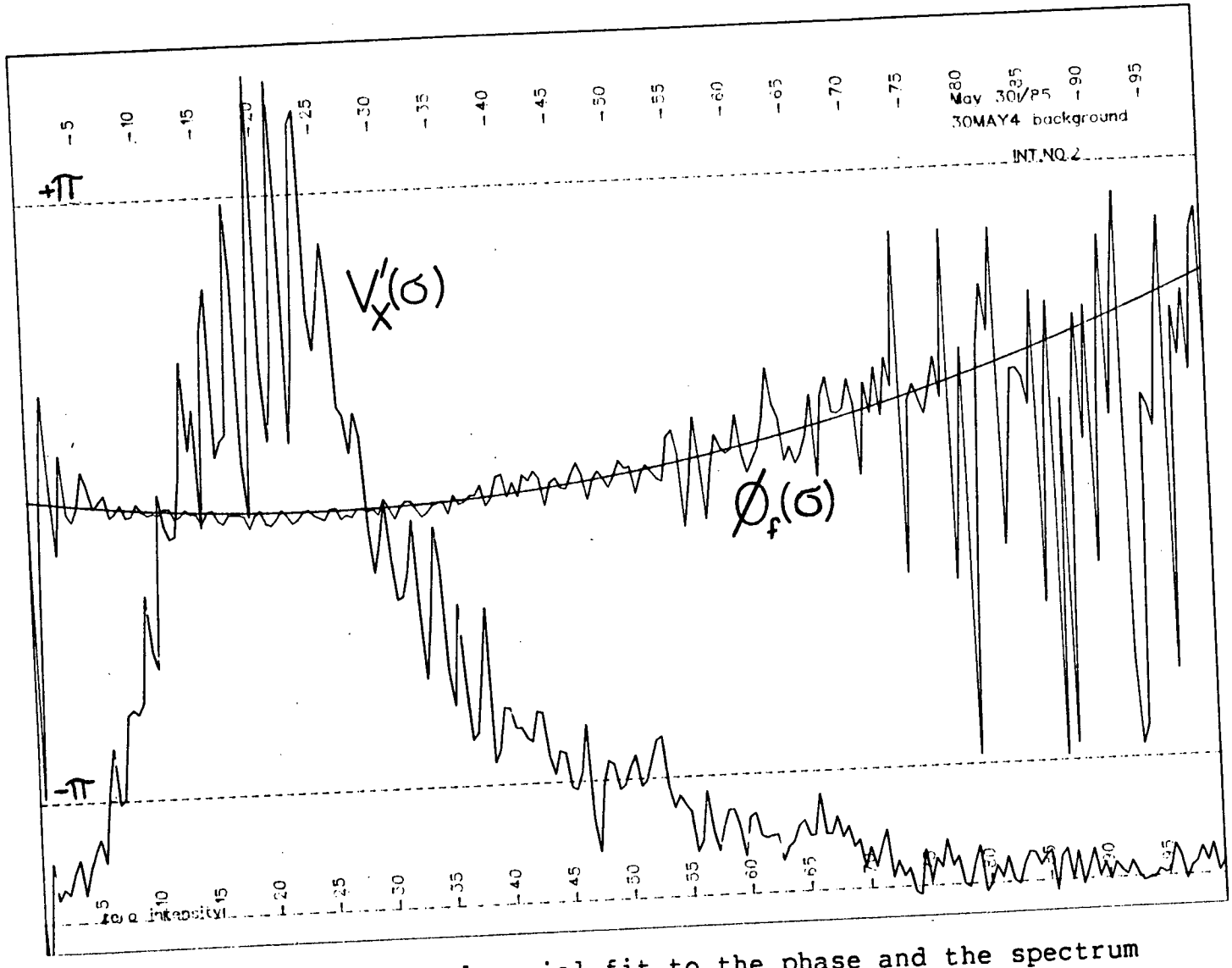

Figure 3 - Polynomial fit to the phase and the spectrum $V_x'(\sigma)$

The spectrum obtained $V_X'(\sigma)$ can be either positive or negative. This differs from the modulus spectrum which is the magnitude of $|\vec{V}| = \sqrt{V_X^2 + V_Y^2}$ and is always positive. The noise in $V_X'(\sigma)$ is the linear sum of the noise in V_X and V_Y, whereas the noise in the modulus is added in quadrature. When spectra $V_X'(\sigma)$ are averaged the signal to noise ratio improves; when spectra $|\vec{V}|$ are averaged the base level increases because the noise is always positive and therefore the intensities obtained are not correct.

A problem in the performance of the interferometer was discovered during these tests. Experiments were conducted with an optical high frequency cutoff of about 40 cm^{-1}, and yet spectra appeared at 90, 150, and 200 cm^{-1}. The peak intensities of the "alias" spectra were about one or two percent of the peak of the true spectrum intensity. Moreover, these "alias" spectra were images or mirror images of the spectrum measured between 2 and 40 cm^{-1}. Dr. Gush demonstrated that this aliasing was due to uneven sampling of the interferogram. The fourfold repeating of the real, low frequency spectrum indicated a fourfold periodicity with respect to the sampling error.

To eliminate the sampling error, direct measurement of the mirror carriage position is made by a capacitance gauge. The position of the mirrors is a linear function of a measured voltage. However, the 12 bit A-D conversion is not sensitive enough to detect deviations from even sampling. The data from the capacitance gauge is divided up into four

sets of data. Each set corresponds to the first, second, third, or fourth sample in a repeating cycle of four samples. Each set is then fit with a line of voltage as a function of sample number. The data is recomposed into a more accurate set of fitted voltages per sample number, where the digitization noise of the measurements is now removed. The interferograms are now a function of voltage, where the sampling intervals between points are uneven, but known. Computer interpolation of the interferogram yields a new interferogram which is a function of even interval sampling. This new interferogram is Fourier transformed according to the above procedure and the aliasing observed prior to the capacitance measurement is effectively eliminated. The peak intensity now of the "alias" spectrum is approximately 0.3 percent of the real spectrum peak intensity. This is comparable to the noise level of the spectrum.

The absorption measurements of liquid nitrogen and oxygen utilized not only the interferometer and associated data aquisition and analysis schemes, but also required a specially designed sample cell. Essentially, the cell is a sample space between two vacuum spaces. Its basic purpose is to contain a 1 cm slab of a liquified gas at liquid nitrogen temperatures, and to prevent condensation on the sample chamber windows. The thickness is chosen so that a liquid nitrogen sample absorbs about 50% of the incident light at a frequency of 50 cm^{-1}, based on the work of Buontempo et al (31). The aperture of the cell is large in order to pass as

much of the interferometer beam through the sample as possible. The window material is TPX which is relatively transmissive in the far-infrared and the optical regions (28). Nylon is chosen for the cell body because it is easily machined, is relatively strong, and has a thermal coefficient of expansion similar to the windows.

The cell cooling system is extremely simple. The cell is built into a styrofoam box which is filled with liquid nitrogen. In practice, filling the box is done gradually to avoid cracking the windows or glue joints.

Construction of the vacuum windows is also simple, but it is not particularly rugged. Low temperature vacuum windows are in general rather tricky and the solution here was to epoxy the TPX windows to the nylon cell body. The cell body was turned down on a lathe to an annulus 2 inches in diameter and 0.025" thick. This thin ring extends 0.5" from either end of the window cylinders. It accomodates differences in contraction between TPX and nylon. A slot in the windows of 0.030" thickness and half the window depth is cut to exactly fit the thin ring of the window cylinder. Armstrong A-271 epoxy is then used to fix the windows to the nylon cell. This system works pretty well if the cell is cooled slowly, however sudden cooling will break the windows or the joint (see accompanying cell drawing fig. 4).

The two vacuum window sections are joined to a central section which is the sample space. Indium O-rings seal these window sections to the central section. A stainless steel

tube is inserted into the central section to fill the sample chamber. The central section is wrapped in aluminum tape to insure that the temperature of the sample chamber is uniform.

The gas handling system consists of the sample cell, a pressure gauge, the sample gas cylinder, and a vacuum pump. Initially the vacuum spaces are pumped out with a diffusion pump and then closed off. The sample chamber and gas lines are then evacuated. After the styrofoam box is filled with liquid nitrogen and the cell is cold, gas is admitted into the sample chamber. The gas condenses and slowly fills the chamber. The sample chamber is cleared by slowly evacuating it with the roughing pump.

The placement of the sample cell in the interferometer optical path is depicted in fig. 5. The cell entrance window is placed approximately 15 cm from the analyzing polarizer. This puts the cell exit window about 32 cm from the TPX condensing lens. The interferometer beam converges

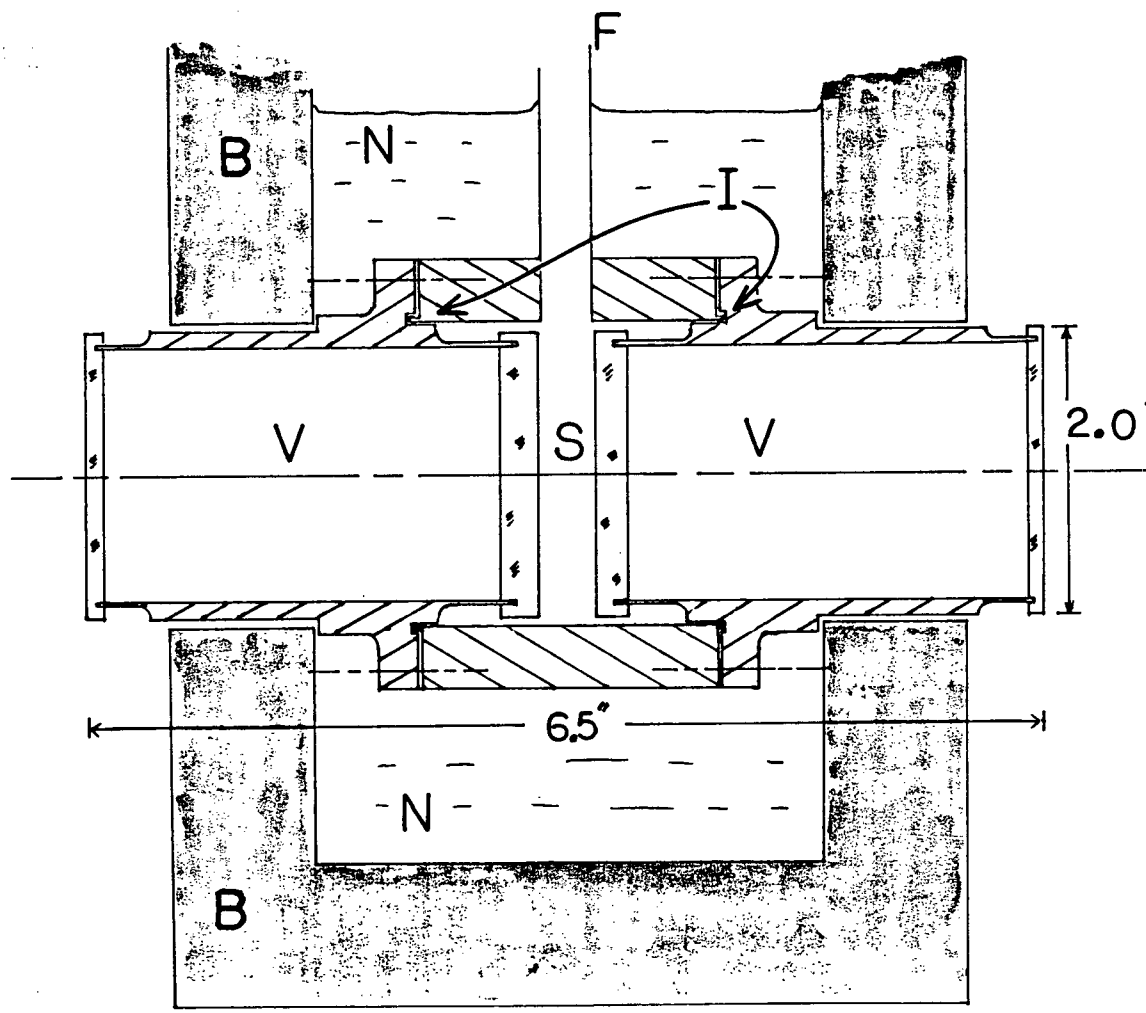

Figure 4 - Liquified gas sample cell
Components are: vacuum spaces V, sample chamber S, liquid N_2 bath N, styrofoam box B, fill tube F, indium O-rings I.

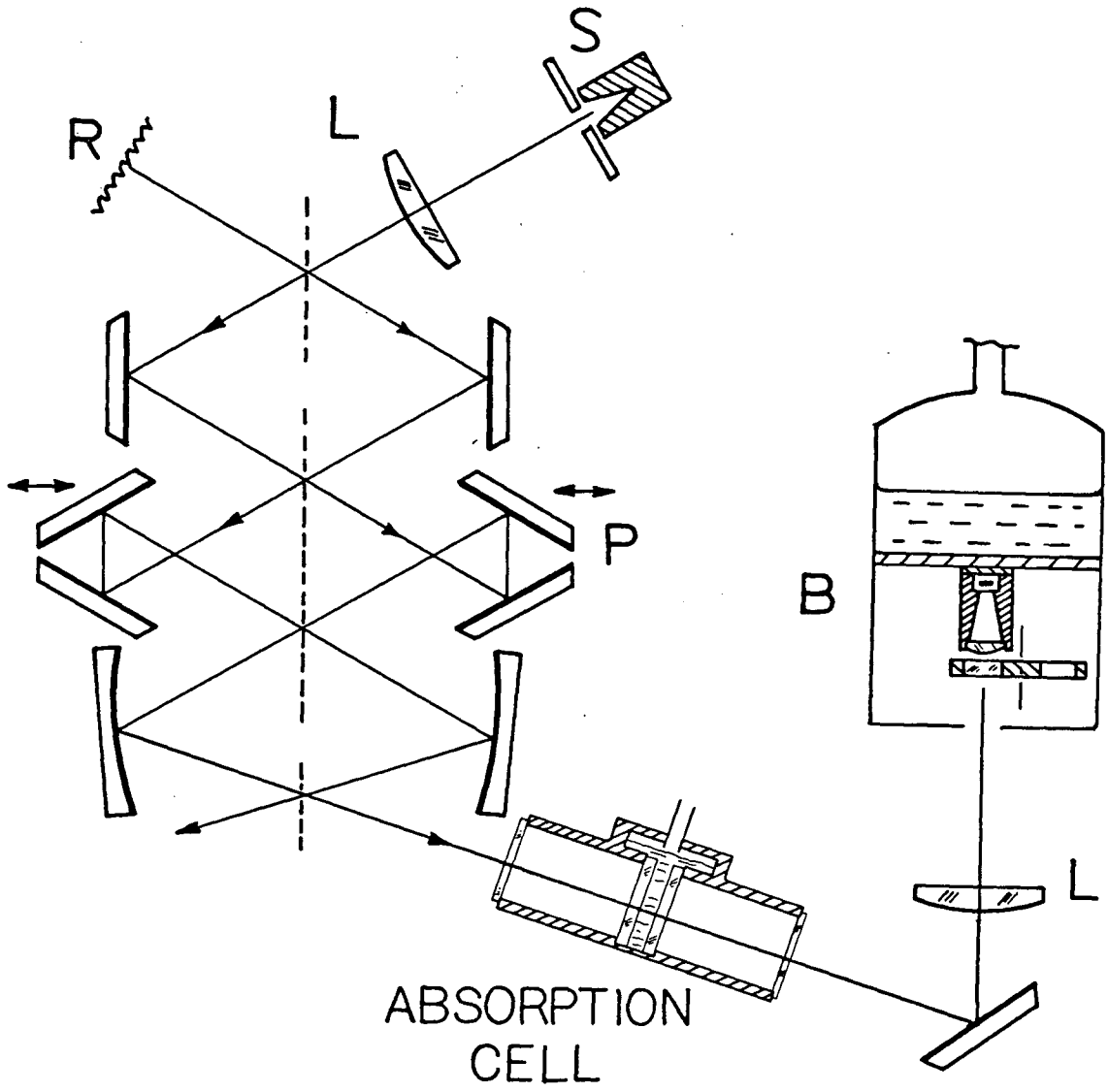

Figure 5 - Diagram of the optical system
P, the interferometer (the dotted lines represent the wire grid polarizers, the arrows indicate the mirror movement); L, TPX lens; S, a 600 C blackbody source; R the room at 23 C, a second blackbody source; B, the liquid helium cooled bolometer; C, the sample cell.

within the cell, the beam diameter at the cell exit window is about 7 cm. The cell window diameter of 5 cm therefore passes half the light from the interfermeter assuming a beam of uniform intensity. The transmission of all the TPX windows at 30 cm^{-1} (roughly midrange in the spectrum) is about 50%. Therefore, the total light transmitted by an empty cell is about 1/4 of the light transmitted by the interferometer system with no cell present. This is generally confirmed by comparing the total intensity falling on the detector with the cell in the path to the total intensity with no cell in the optical path.

One final feature of the experimental procedure is the purging of the optical path. Water vapor is a very strong absorber in the far-infrared frequency region and it is desirable to remove it as much as possible. The optical system was enclosed by a polyethylene tent purged with nitrogen vapor by pouring liquid nitrogen into an uninsulated container within the tent. For the high frequency measurements, additional nitrogen gas was blown into the tent from a gas cylinder and this was more effective at eliminating the water vapor lines than using liquid N_2 alone. One problem with purging is that the water vapor content within the tent varies from measurement to measurement. Since the absorption coefficient is based on a ratio of background to sample spectra, the variation in purging can produce strong features in the absorption curves at the frequencies of water vapor absorption lines.

3.2 Experimental Results

A portion of the experimental work of this thesis is a measurement of the absorption of far-infrared light by liquid nitrogen and liquid oxygen. As previously discussed this absorption is predominantly due to $\Delta J = 2$ rotational molecular transitions arising from collision induced dipole moments. A considerable amount of investigation has been carried out on collision induced absorption in gases, both theoretical and experimental, especially on H_2, N_2, and rare gas mixtures. However, not much far-infrared work has been done on liquids in general, or on oxygen in particular. A review of previous experiments which are pertinent to the present studies follows.

There have been numerous measurements of the spectrum of gaseous nitrogen since the discovery of collision induced absorption. The experiments of Bosomworth and Gush (30) using a Fourier transform spectrometer are widely quoted and compared to more recent measurements under different conditions. They measured the absorption coefficient of gaseous nitrogen 300 K, from 40 to 350 cm^{-1} in the density range 20.9 to 33.6 Amagat. Measurements in the gas have also been made by Buontempo et al (31) at 124K, and Dagg et al (32) and Stone et al (21) over a wide temperature range.

In addition, there are two published measurements of the far IR absorption of liquid nitrogen: an early experiment of Stone and Williams (33) and a later experiment by Buontempo et al (31).

The Stone paper describes the transmission of liquid nitrogen over the frequency band 30 - 200 cm^{-1}. These measurements use a grating spectrometer purged with nitrogen gas. The liquid nitrogen was contained by two cells, one 12.5 mm thick, the other 2.5 mm thick. The ratio of the spectra obtained through each cell is therefore the transmission of a 10 mm slab of liquid. An absorption peak near 75 cm^{-1} was observed. A major problem with this measurement is that ice crystals were observed in some of their liquid samples. Since water is strongly absorbing in the far-infrared, the reliability of these results is questionable.

Buontempo et al (31) have measured the transmission of liquid nitrogen at a temperature of 66K, using a Michelson interferometer in the frequency region 25 to 250 cm^{-1}. In addition they measured the absorption coefficient of the gas at 300K and 124K. The cell for the liquid experiment was roughly 10 mm long and had mylar windows. Their cell length was uncertain since the windows bulged outwards when the cell was full. Consequently they were unable to calculate an accurate absorption coefficient. In spite of this serious deficiency, it remains the best available measurement of liquid nitrogen. Background spectra were obtained with an evacuated cell or with a cell filled with liquid argon. Filling the cell with liquid argon compensates for the change in index of refraction between an empty cell and one that is full of liquid. They state that the liquid nitrogen

transmission results were the same using either background.

Their work shows that in general, the absorption in the liquid is similar to that in the gas. The peak absorption in the liquid phase at 66K occurs at 60 cm^{-1}, whereas in the gas at 124K, it occurs at 70 cm^{-1}. A difference between the gas and liquid spectra is that the integrated absorption coefficient divided by the square of the density is less for the liquid than that estimated for a gas at the same temperature. Also the liquid spectrum shows a stronger absorption at high frequencies than the gas spectrum. These features may be accounted for in part by considering that in the liquid interactions are taking place between more than just isolated pairs of molecules (unlike the low density gas). The quadrupole fields of many neighboring molecules will be superimposed on the site of the molecule in which a dipole is induced. This superposition decreases on average the magnitude of the electric field at this site as the molecules are considered to be randomly oriented. The liquid's higher absorption in the high frequency region may be ascribed to double transitions, where each of a pair of molecules undergoes a rotational transition. In this case, the dipole moment is not cancelled, as it is for single transitions, by the proximity of neighboring molecules.

The microwave absorption at 2.3 cm^{-1}, of liquid nitrogen has been measured by Urbaniak et al (34). This measurement is at a frequency where far-infrared techniques become inaccurate and hence is important in defining the spectrum in

the low wavenumber region.

In the case of liquid oxygen, no previous work in the far-infrared has been published. Even for gaseous oxygen there are few far-infrared experiments except that of Bosomworth and Gush (30). The collision induced rotational spectrum of gaseous oxygen at 300K and densities between 35 and 75 Amagat was measured over the frequency region 20 - 400 cm^{-1}. Their work shows an oxygen absorption peak at approximately 110 cm^{-1}, about the same as their nitrogen absorption peak. The far-infrared absorption of gaseous oxygen is about 10 times less than gaseous nitrogen. The collision induced fundamental vibration-rotation band of oxygen was measured over the range 1300 - 1800 cm^{-1} by Shapiro and Gush (35). The gas temperature was 300K and the density was in the range 40 - 60 Amagat. In their measurement, the rotational transitions are observed as side bands on the fundamental vibrational transition at 1553 cm^{-1}.

Measurements of the far-infrared absorption of liquid nitrogen and oxygen were performed using the aforementioned interferometer and sample cell. Two sets of measurements covered the frequency regions, 2 - 40 cm^{-1} and 2 - 80 cm^{-1}. The high frequency cutoff in the first case is determined by the optical filters in front of the detector (see Section 3.1). The cutoff in the second case is determined primarily by the absorption of TPX, the material used to make the cell windows and condensing lenses. Measurements of the absorption of TPX (28) show that the transmission is:

$$T = e^{-0.01 \nu t}$$

where t is the thickness of the TPX and ν is the frequency. The thickness in the optical path here was ~5 cm, so the transmission through the optical system at 80 cm^{-1} is less than 2%. In fig. 6 a background spectrum divided by σ^2, in order to normalize the intensity of the blackbody source, is plotted with the transmission of the various filters and TPX of the optical system. The high frequency cutoff of the spectrum is well matched by the transmission of the combined elements of the optical system.

The goal of these experiments is to measure the absorption coefficient $A(\sigma)$ of the two liquified gases (eqn. 2.1). To do this the following experimental procedure was adopted. First, background spectra were measured with the sample cell empty. Next, the cell was filled with liquid by condensation from the gas and spectra were taken. Finally, the cell was emptied and the background spectra were repeated. Each spectral measurement set consists of about 2 or 3 sets of 28 interferograms. Each interferogram was transformed and phase corrected and then all 56 or 84 spectra were averaged. The background spectra used in calculating $A(\sigma)$ are averages of about 112 or 140 background spectra, half taken before and half after the sample spectra. It took approximately one hour to condense gas in the cell and one hour to evacuate the cell with the roughing pump.

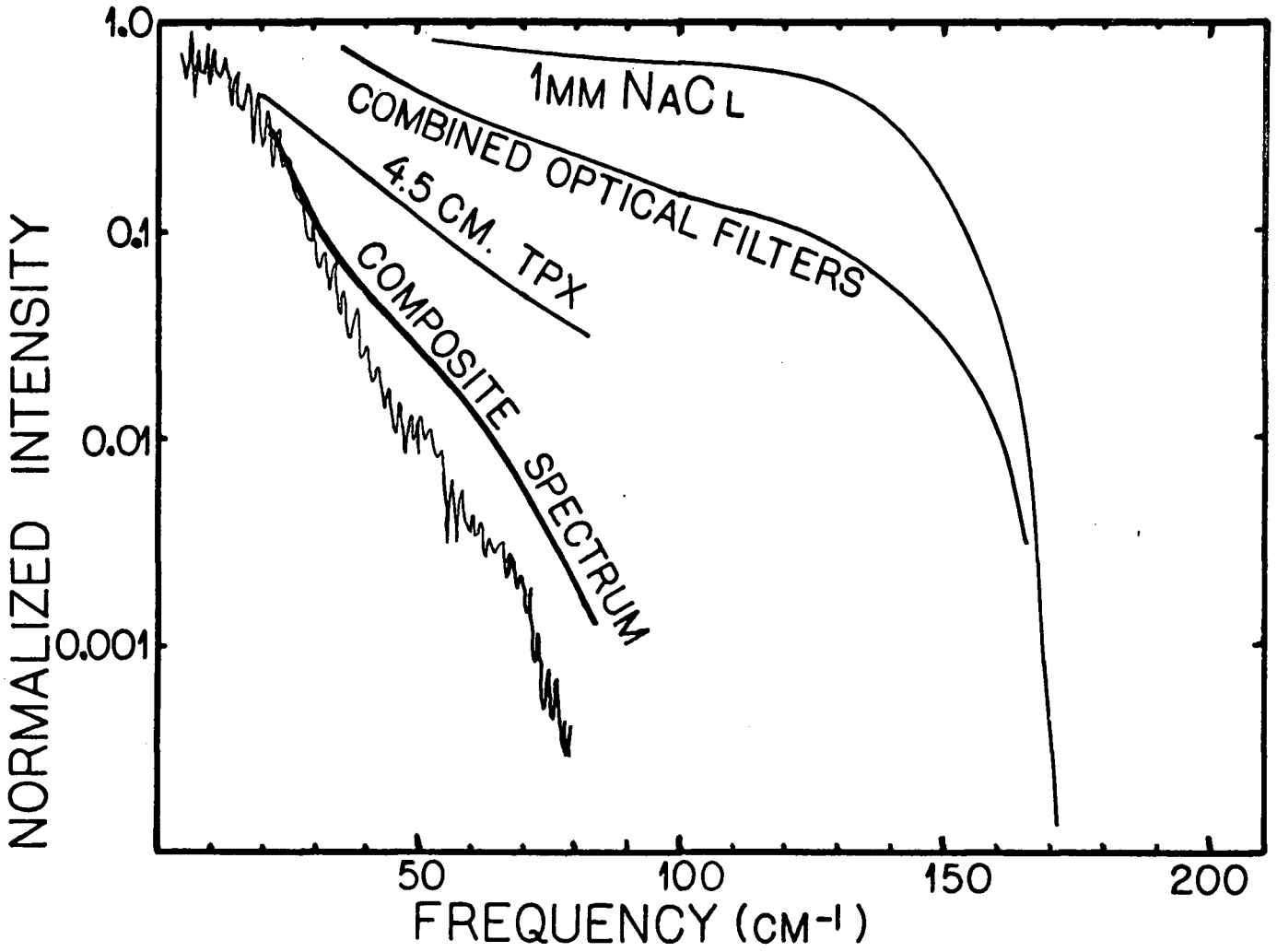

Figure 6 - High frequency cutoff of optical system
Plotted are: a background spectrum/ ; transmission of: 1 mm NaCl, mylar and polyethelene combined filters, 4.5 cm TPX; and a composite transmission spectrum of all these elements combined

This long period between background and sample spectra led to two serious problems. First, the temperature of the bolometer drifted slightly during this period leading to changes in the measured spectral intensity. In addition, the purging of the optical path with nitrogen vapor was not exactly the same from one measurement to the next. This defect is particularly noticeable in the oxygen spectra where the absorption is low, and pronounced water vapor lines may be observed at 18, 25, 36, and 40 cm^{-1}. These lines are due to imperfect cancellation of atmospheric features in the ratio $I_B(\sigma)/I_S(\sigma)$.

An accident happened during the high frequency experiments in which the vacuum windows on the cell were cracked by a spill of liquid N_2. However, the cell worked in spite of this and no frost was observed on the windows as the optical path tent was being well purged with not only evaporating liquid nitrogen, but also with flowing nitrogen gas.

The ratio of background to sample spectrum needs to be taken to obtain the absorption coefficient. However, the transmission of the sample cell when it contains a non-absorbing fluid is greater than when it is empty, since reflection losses at the boundary between the TPX windows and the sample area are less. If interference of light paths reflecting back and forth in the sample region is neglected, the transmission of light at normal incidence, from a medium of index n_1, through a medium of index n_2, and into a

medium of n_1 is:

$$T = \left[\frac{4 n_1 n_2}{(n_1 + n_2)^2} \right]^2$$

Here n_1 is the index of refraction of TPX, and n_2 is the index of of the vacuum or a liquid sample. The index of refraction n can be obtained from the permittivity of a dielectric medium.

$$n = \frac{c}{v} = c\sqrt{\epsilon\mu} = \sqrt{\frac{\epsilon\mu}{\epsilon_0\mu_0}}$$

$$\therefore n \simeq \sqrt{\frac{\epsilon}{\epsilon_0}}$$

where c is the speed of light in vacuum, v is the speed of light in the dielectric, ϵ and μ are the permittivity and permeability of the medium, and ϵ_0 and μ_0 are the permittivity and permeability of free space. For most dielectric materials, $\mu = \mu_0$. The index of refraction of TPX is: n = 1.42 (28), therefore the transmission of the empty cell, T_e = 0.941. The table below gives ϵ, n, T_f the transmission of the full cell, and T_f / T_e the ratio of transmission of the full cell divided by empty cell, for liquids N_2 and O_2. The values of ϵ are given in (36) and have been measured in the liquid phase in the microwave frequency region.

	ϵ	n	T_f	T_f / T_e
N_2	1.454	1.21	0.987	1.049
O_2	1.507	1.23	0.990	1.052

Table 5 - Dielectric constant, index of refraction, and transmission of cell for liquid nitrogen and liquid oxygen

To compensate for the change in cell transmission, the sample spectra are divided by T_f / T_e, otherwise a transmission in excess of unity would be observed in the frequency region of low absorption. The results of the low frequency measurements are accurately compensated by the above constants and transmission at low frequency is shifted to unity. The compensation of the high frequency measurements is not so accurate, but it should be noted that in the low wavenumber region, the low frequency measurements are probably more accurate than the high frequency measurements. The optical filtering used for the low frequency measurements produced well tested and reliable low frequency spectra in the course of measuring the optical properties of cold dielectrics (Halpern et.al. 1985).

The absorption coefficient is obtained from measurements of background spectra and sample spectra. The background measured is:

$$I_B = I_o \ (\ 1 - R_e \ ) = I_o \ T_e$$

where I_o is the initial intensity, R_e is the reflection of the empty cell, and T_e the transmission of the empty cell.

The sample spectra measured is:

$$I_S = I_o (1 - R_f) e^{-\alpha t} = I_o T_f e^{-\alpha t}$$

where R_f is the reflection of the full cell, T_f the transmission of the full cell, α the absorption coefficient, and t the sample thickness. The ratio of I_S / I_B then is:

$$\frac{I_S}{I_B} = \frac{T_f}{T_e} e^{-\alpha t}$$

T_f / T_e is calculated above for O_2 and N_2 liquids inside a TPX cell. The absorption coefficient is then:

$$\alpha = \frac{1}{t} \ln \frac{I_B}{I_S'} \quad , \text{where} \quad I_S' = \frac{I_S}{T_f / T_e}$$

The absorption coefficient of liquid nitrogen is displayed in fig. 7. The heavy line is from the set of low frequency measurements, and the light line is from the high frequency measurements. For both sets of measurements the data plotted extends about 10 cm^{-1} higher in frequency than the region of reliable results. Also plotted on this graph are the absorption coefficients of liquid N_2 found by Stone et al, and Buontempo et al, which were obtained from their transmission data assuming a known cell length. The vertical bars are proportional to the unbroadened intensities of absorption by rotational transitions in a pair of nitrogen molecules. These are single transitions which are due only to quadrupolar induction and their intensity scale is arbitrary (see table 3).

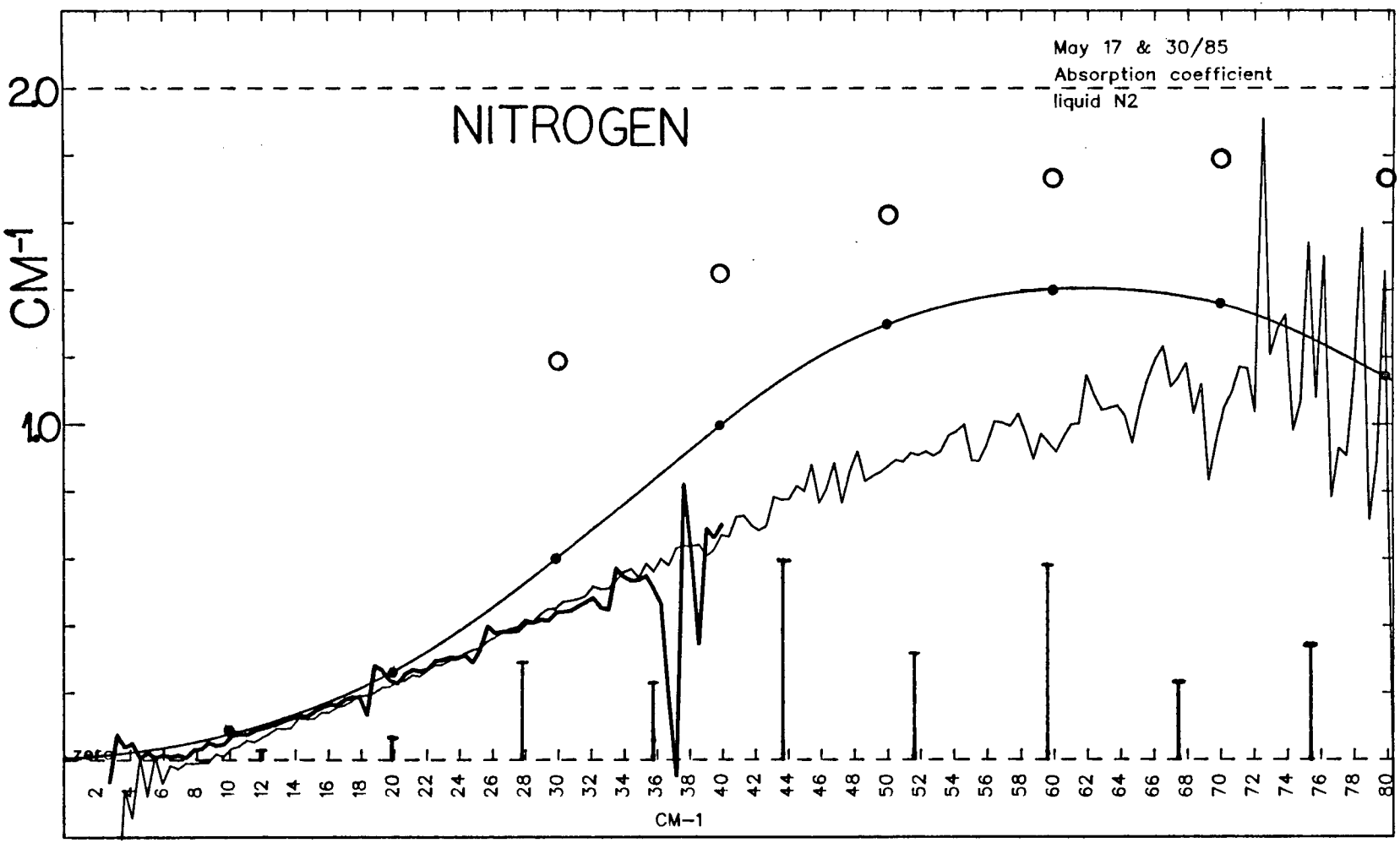

Figure 7 - Absorption coefficient of liquid nitrogen
Heavy line, low frequency measurements; light line, high frequency measurements. Also plotted are results from (31), dots; and (33), open circles; and calculated quadrupolar induced single transition line intensities, bars (see table 3).

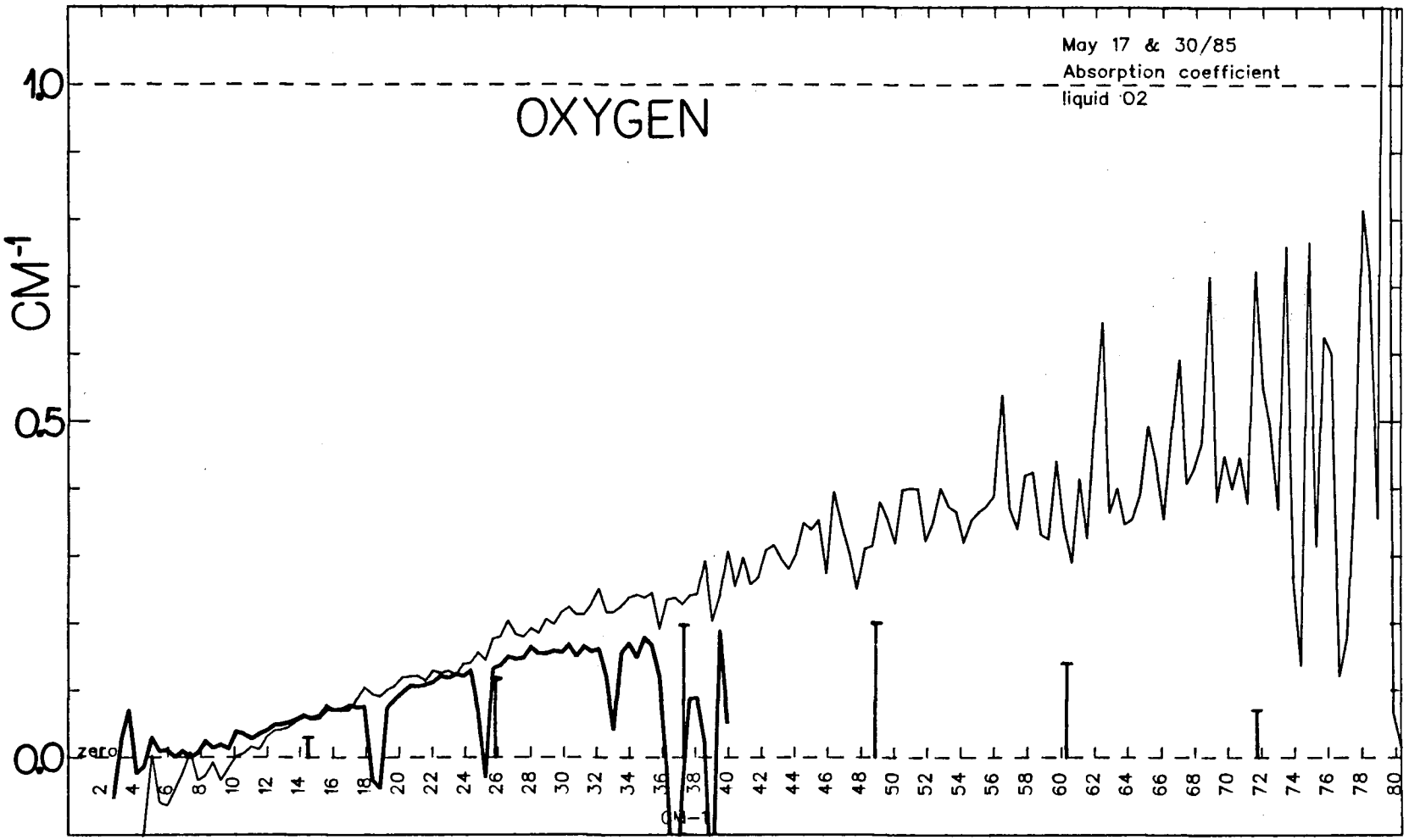

Figure 8 - Absorption coefficient of liquid oxygen
Heavy line, low frequency measurements; light line, high frequency measurements. Vertical bars are calculated quadrupolar induced single transition line intensities, (see table 3).

Figure 7 shows that the absorption coefficient measured in this work is less than that measured by either of the previous experiments. In the case of Stone, this discrepancy may be accounted for by the presence of ice particles in the liquid nitrogen samples which would lead to larger absorption. In the case of Buontempo, if their cell thickness was larger than reported, the absorption coefficient calculated from their data would be reduced. The discrepancy in the shape of the absorption curves remains unexplained. Their absorption curve shows a roll-off starting at 60 cm^{-1}, and a peak near 70 cm^{-1}. The absorption curve fig. 7, clearly does not follow the intensities for binary collisions represented by the vertical bars. The reason for this could be the result of double transitions, as mentioned earlier, or higher order multipole induction processes (37).

The first reported measurement of the far-infrared absorption coefficient of liquid oxygen is displayed in fig. 8. The heavy line is from the low frequency measurements, the light line is from the high frequency measurements. Also shown is a theoretical rotational stick spectrum taking into account only quadrupolar induction and single molecule transitions (see table 3).

The agreement between the low frequency measurements and the high frequency measurements for oxygen is not as good as the nitrogen results. The signal to noise ratio in the oxygen data is also not as good as the nitrogen case, because

oxygen absorbs considerably less than nitrogen for the same path length. Major deviations between spectra and background in the case where absorption is small (and the signal is small) are related to inconsistencies with the purging of the optical path. The absorption coefficient of liquid oxygen is about half that of liquid nitrogen, whereas the absorption coefficient of gaseous oxygen is about one tenth that of gaseous nitrogen (30). The high frequency spectrum does not clearly show a peak, although there appears to be a roll-off at about 60 cm^{-1}. It is clear however, that the observed spectrum does not follow the envelope of the theoretical stick spectrum. For both nitrogen and oxygen, higher frequency measurements encompassing the entire absorption band are desirable. Increasing the cell length to obtain larger absorption would improve the signal to noise ratio at low frequencies, especially for oxygen.

Information on the transition probability between rotational states of the molecules in the liquid can be obtained from the absorption curves by taking into account a frequency factor and the effect of stimulated emission. The probabilities of stimulated emission and stimulated absorption of light due to molecular energy transitions are equal, however since the population of lower energy states is greater than higher energy states for a system in thermal equilibrium, there will be a net absorption of radiation. At liquid nitrogen temperatures, the intensity of emission is about the same as absorption for energy transitions less than

50 cm^{-1}. The line shape function is proportional to the probability of molecular transitions between states separated in energy by $E = hc\sigma$, and is related to the absorption coefficient by:

$$G(\sigma) = \frac{A(\sigma)}{\sigma(1 - e^{-hc\sigma/kT})}$$

Here dividing by σ accounts for the contribution of frequency to the intensity of absorption and dividing by $(1 - \exp(-hc\sigma/kT))$ accounts for the measured light intensity due to stimulated emission.

The following graphs, figs. 9 and 10, show the line shape function for liquid N_2 and liquid O_2. The microwave point from (34) is also plotted, and seems relatively consistent with the present N_2 measurement if the higher frequency part of the curve is continued to zero wavenumbers. Both curves show that at lower frequencies there is a higher transition probability than at higher frequencies. There is a large increase in the line shape function of nitrogen gas at the low frequencies due to collision induced translational absorption (31)(32). The absence of any large increase in the liquid line shape function might indicate that translational motion is inhibited by the density or molecular clustering.

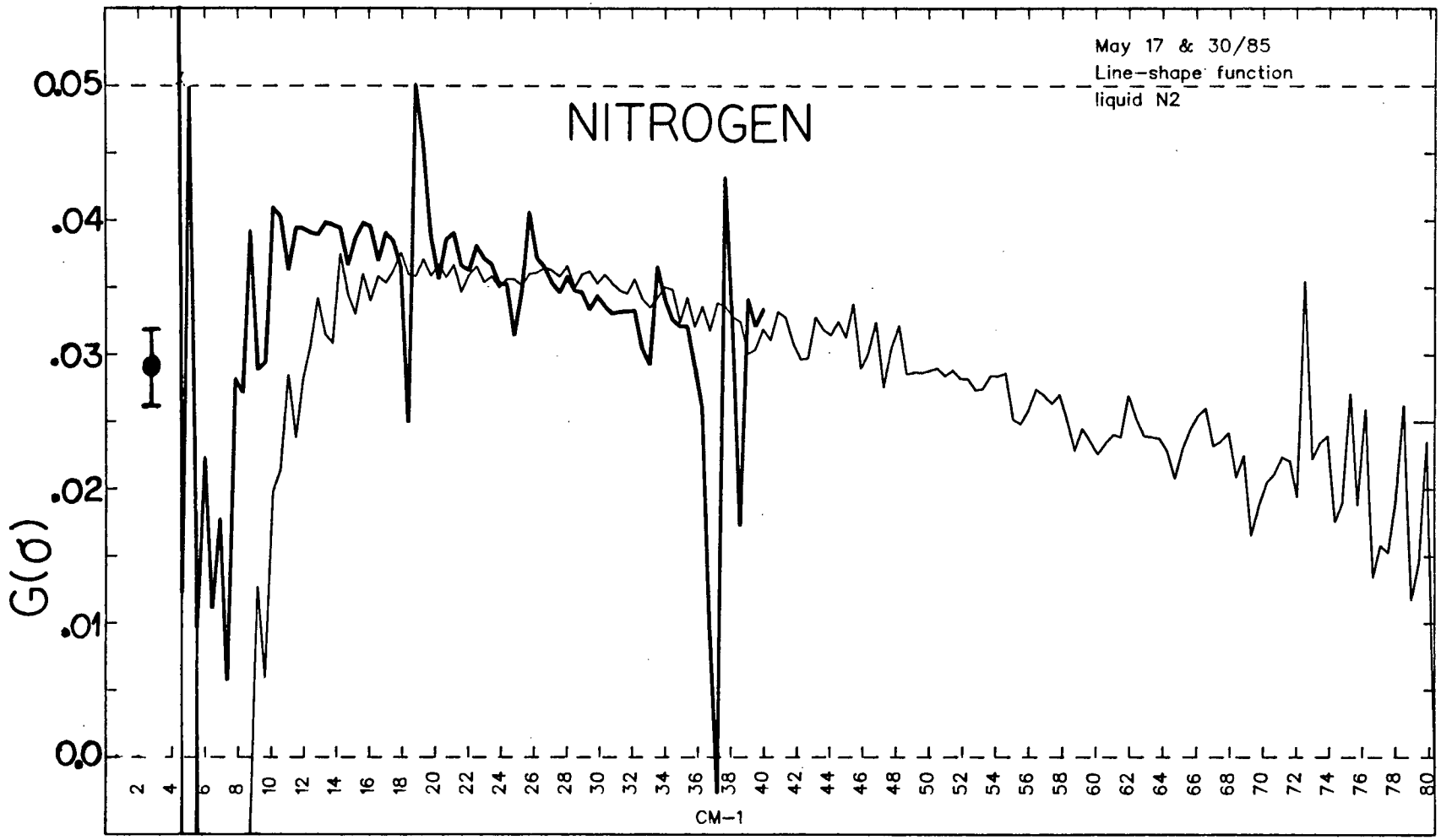

Figure 9 - Line shape function of liquid nitrogen
Heavy line, low frequency measurements; light line, high frequency measurements; microwave point from (34) is also plotted.

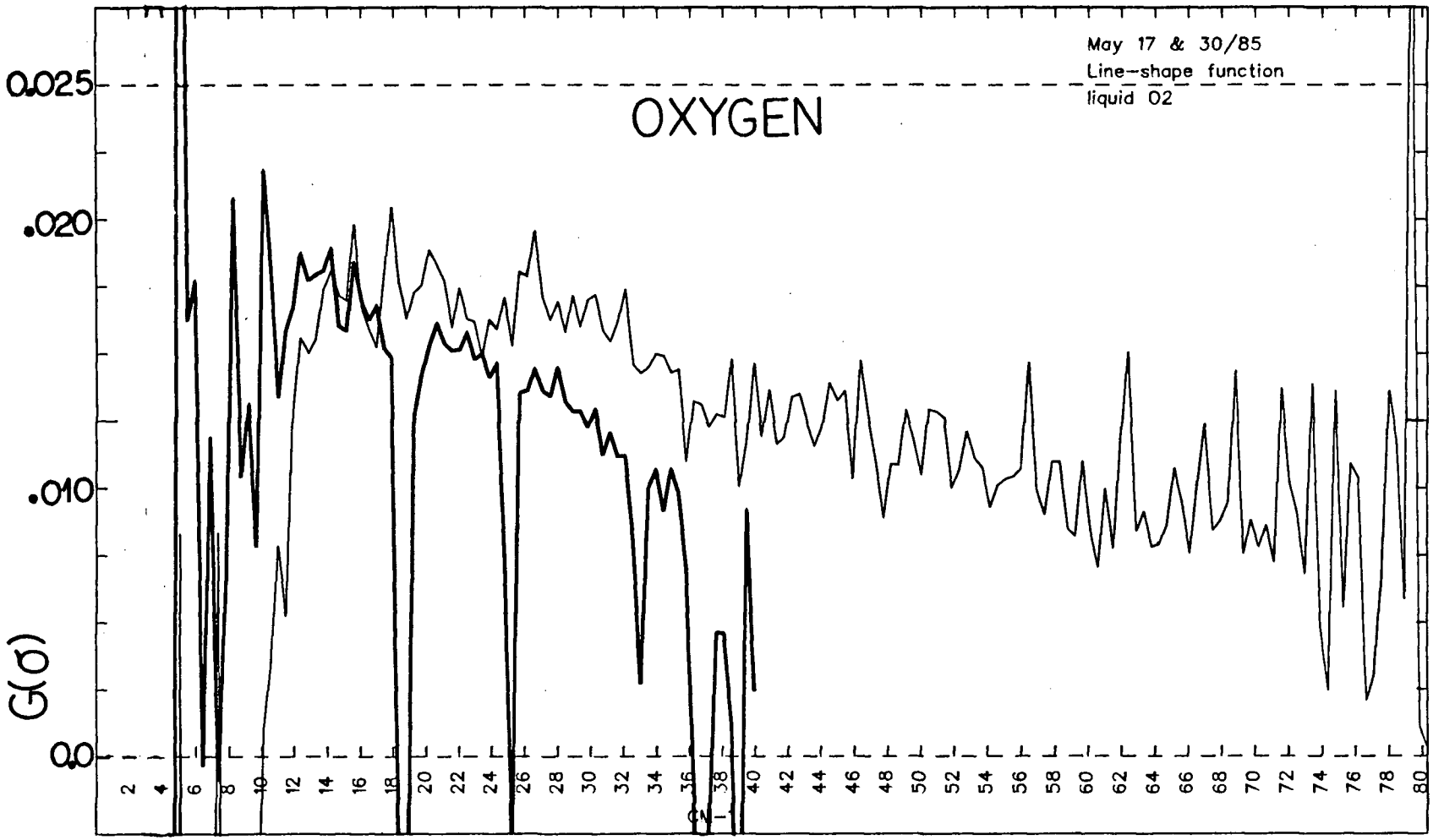

Figure 10 - Line shape function of liquid oxygen
Heavy line, low frequency measurements; light line, high frequency measurements.

The 5 - 8 cm^{-1} dip in the nitrogen low frequency line shape curve (heavy line) may be similar to a dip observed at low frequencies in the translational absorption of hydrogen gas (38). For hydrogen gas, this dip is attributed to a change in sign of the dipole moment between successive molecular collisions. In the present case, since the absorption is quite low, this region of the line shape function is very sensitive to small errors in the background spectrum. By increasing the background by 2% (within the error of these measurements) this dip is eliminated and therefore it will be necessary to improve the accuracy of these measurements to demonstrate the validity of this feature of the line shape function.

IV. LOW TEMPERATURE MULTIPLE PASS FAR-INFRARED ABSORPTION CELL

In order to investigate H_2 in a situation similar to astrophysical environments, a low temperature, multiple pass, optical absorption cell was designed. The design concept is being augmented and translated into detailed mechanical drawings by Alex Leung. It is anticipated that the cell construction will begin shortly.

The first use of the absorption cell will be to measure the far-infrared spectrum of hydrogen dimers $(H_2)_2$ at high resolution. The existence of these dimers has been confirmed by observations of the collision induced absorption in the fundamental band (2)(3), but no previous far-infrared measurements have been made. Experiments are planned to examine the translational spectrum of hydrogen from approximately 20 - 200 cm^{-1} using a Fourier transform Michelson interferometer as well as the dimer absorption at the $S_0(O)$ hydrogen line at 354.4 cm^{-1} using a laser diode spectrometer.

The binding energy of H_2 dimers is of the order of a few cm^{-1} and they are easily dissociated by collision. To observe dimers the gas pressure must be less than a few atmospheres, and the temperature must be less than about 50K. Since the absorption is expected to be weak, it is desirable to have as long an optical path length as is practical. This cell design, a low temperature multipass "White cell" (39) fulfills both these requirements.

A White cell essentially consists of a field mirror and 2 folding mirrors, (twin mirrors) all of the same radius of curvature. The distance between the mirrors is equal to the radius of curvature, and the path length can be adjusted by changing the angle between the twin folding mirrors. The path length obtained is:

$$L = (2\ell \times n) + 2$$

where l is the length of the cell and n is the total number of spots on the field mirror. To obtain the longest path length, the folding mirrors are adjusted until the spots on the field mirror are as close as possible without overlapping.

A notable feature of this new cell is that it has an f/10 optical system, this is a "faster" beam than other low temperature White cells described in the literature (40)(41)(2). Because very low optical frequencies will be used in these experiments, the light beam will be significantly diffracted by the folding mirrors, and this will limit the maximum attainable path length. Diffraction from these mirrors is minimized by designing them to be as large as possible. To obtain long path lengths, for a given cell length, the field mirror must also have a large diameter in order to stack up as many spots as possible. An optical system has been designed where the field mirror has a diameter of 20 cm and each folding mirror a diameter of 10 cm. All mirrors have a radius of curvature of 1 meter.

Although a longer path length would be possible if the cell were larger, difficulties with a previously constructed 3 meter cell indicated that it is more practical to build and operate a 1 meter cell.

The maximum path length attainable with this cell is determined by the size of the diffraction spot and the number of these spots that can be placed onto the upper row of images on the field mirror. The width of the field mirror between the entrance and exit slots is 16.8 cm. The table below gives the wavelength, the diffraction spot size diameter, the number of spots on the top row, the total number of spots, and the total path length of the cell for low frequencies of light.

σ	λ	d	#top	#total	path length
20 cm^{-1}	0.5 mm	1.22 cm	13	27	56 m
30 cm^{-1}	0.33 mm	0.85 cm	19	39	80 m

Table 6 - Diffraction spot size and maximum path length for low optical frequencies

The diffraction spot size calculated above assumes that the input to the cell is a point source. This is not the case, as the transfer optics magnify the interferometer output aperture by a factor of 2. The input spot size is 0.6 cm, and the maximum path length using this interferometer, discounting diffraction, is 116 meters.

The photograph, fig. 11 indicates the major components of the cell system. It consists of a 1 meter long low temperature optical cell, which is made of stainless steel and is electroplated with copper. The mirrors are mounted on invar beams within the cell. Invar has a low thermal contraction, so the distance between the mirrors stays constant as the cell cools. Surrounding the cell are two polished copper radiation shields. The cell, shields, and transfer optics are all contained in a vacuum tank. Helium vapor circulates through copper tubes soldered to the cell to cool the sample gas. The helium vapor then circulates around the copper shields to extract the heat input to the shields from thermal radiation. A sophisticated mechanical feedthrough scheme allows for adjustment of the cell optics even when the cell is cold.

The input transfer optics have been designed to match the f/10 optical cell to an f/5 interferometer and also to an f/11 laser diode spectrometer. The output transfer optics match the cell light beam to a liquid helium cooled bolometer which accepts a light cone of about f/4.5. The vacuum windows of the optical cell are crystal quartz lenses (for 20 - 200 cm^{-1}, CsI for 200 cm^{-1} and up) and are designed to image the transfer optics mirrors onto the cell folding mirrors. By doing this extreme rays, due to an interferometer aperture of finite size, are propagated through the optical system without vignetting.

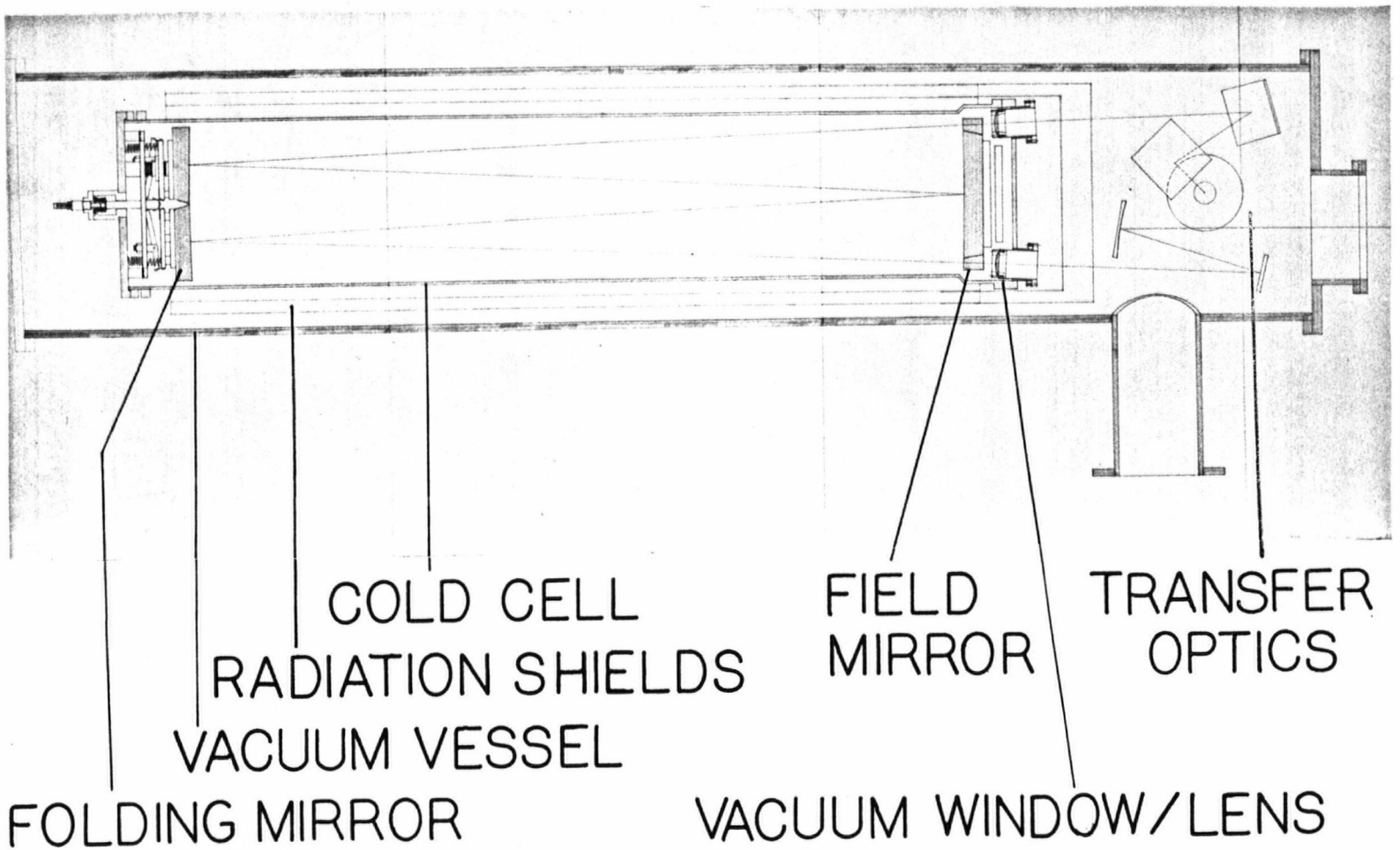

Figure 11 - Diagram of the low temperature multipass absorption cell

Mirrors have 1 m radius of curvature and are spaced 1 m apart, low temperature cell is 1.2 m long and 20 cm in diameter, Vacuum tank is 1.75 m long and 35 cm in diameter. Drawing shows minimum optical path of 4 m. Liquid helium cooled bolometer sits above transfer optic area (out of the plane of the diagram).

A computer calculation has demonstrated that this cell design is practical from a cryogenic standpoint. The cell will be cooled by helium vapor obtained from the evaporation of liquid helium. The calculation provides an estimate of the rate of helium consumption, and is based balancing the heat inputs from radiation and conduction with the heat output due to increasing the enthalpy of the helium vapor coolant. This calculation is based on a similar one used by Prof. Gush to estimate the helium consumption of the rocket borne, liquid helium cooled interferometer. A simplified presentation of this calculation is given by the following drawing and discussion.

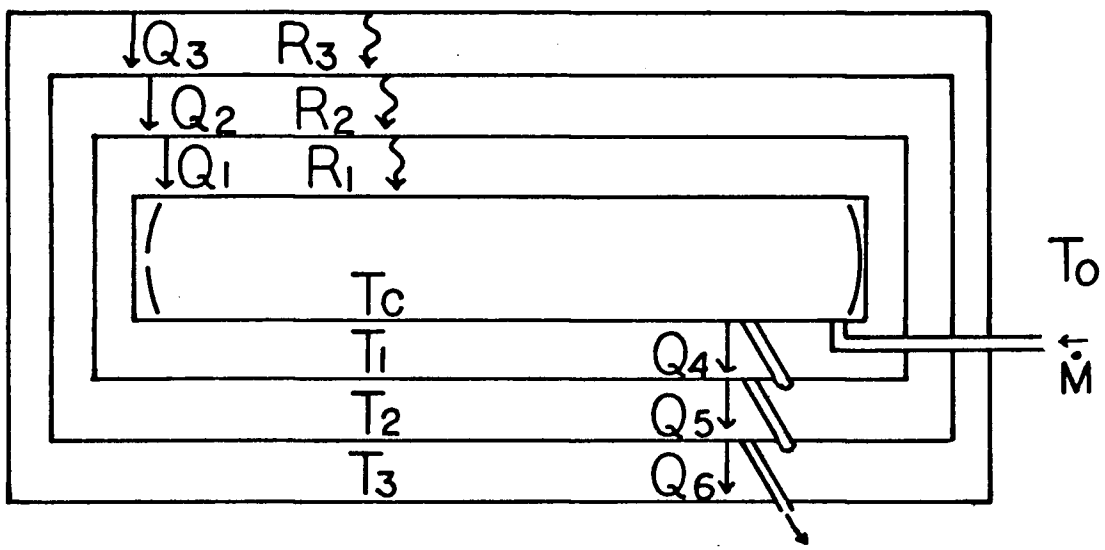

Here T_c , T_1 , T_2 , T_3 , T_o are the temperatures of the cell, shield 1, shield 2, the vacuum tank, and the liquid helium reservoir, respectively. Q_1 , Q_2 , Q_3 are the heat flows by conduction, from shield 1 to the cell, from shield 2 to shield 1, and from the tank wall to shield 2, respectively. R_1 , R_2 , R_3 are the radiant heat inputs, again from shield

1 to the cell, from shield 2 to shield 1, and from the tank wall to shield 2. Q_4 , Q_5 , Q_6 are heat flows absorbed by the changes in enthalpy of the cooling vapor, from the cell to shield 1, from shield 1 to 2, and from shield 2 to room temperature. The heat balance equations for this model follow.

At the cell: $Q_1 + R_1 = Q_4$

At shield 1: $Q_2 + R_2 + Q_4 = Q_5$

At shield 2: $Q_3 + R_3 + Q_5 = Q_6$

$Q_{1,2,3}$ are heat flow rates, in Watts, into the cell and shields due to conduction. For example, Q_1 is given by:

$$Q_1 = K_{1C} (T_1 - T_C)$$

where K_{1C} is the thermal conductivity of the support structure of the optical cell and $(T_1 - T_C)$ is the temperature difference between shield 1 and the cell. The heat flows extracted from the cell and shields by the helium vapor are $Q_{4,5,6}$. For example, Q_4 is given by:

$$Q_4 = \dot{m} (L + C_p (T_C - T_0))$$

where $\dot{m}$ is the mass flow rate of the cooling gas, L is the latent heat of evaporation of helium and C_p is the specific heat of helium. The radiant heat inputs, $R_{1,2,3}$, are due to blackbody radiation from structures at higher temperatures to structures at lower temperatures. For example R_1 is given

by: (42)

$$R_1 = \sigma A_c E_{1c} (T_1^4 - T_c^4)$$

where σ is the Stefan-Boltzmann constant, A_c is the surface area of the cell, and E_{1c} is the emissivity which takes into account the emissivities of the cell wall and shield 1, and their geometry.

The computer calculation solves simultaneously for the three unknowns of this system: T_1 , T_2 , $\dot{m}$, given inputs of the emissivities, thermal conductivities, and desired cell operating temperature. The results for the cell operating at a temperature of 20K are: T_1 = 144K, T_2 = 243K, $\dot{m} = 0.435 * 10^{-2}$ gms/sec, this is a liquid helium loss rate of 3.08 liters per day. This is the expected helium consumption once the cell has reached the operating temperature; additional helium will be necessary to cool it down initially.

The cell cryogenic design attempts to minimize thermal conduction from room temperature to the cell by using low thermal conductivity materials and long path lengths in the cell suspension system. The radiant heating is also minimized by designing the cell and shields to be as reflective as possible. The stainless steel optical cell is electroplated with copper to increase the thermal conductivity. This will insure temperature uniformity across the cell and will conduct heat more efficiently to the cooling vapor.

The problem of diffraction as mentioned above is crucial to the performance of this cell in the far-infrared. A calculation of the spherical aberration and astigmatism (41) of the light beam at maximum path length shows that these aberrations are negligible compared to diffraction. In order to understand to what extent diffraction distorts the optical beam an experimental investigation was undertaken.

The problem simply stated is: Does the beam spot size increase with successive reflections in the mirror cell? This discussion begins by following the light beam through the cell.

The transfer optics inject an f/10 beam into the cell so that the beam is focussed at the field mirror edge and then fills one of the twin mirrors. The twin mirror focusses the beam back to a small spot on the surface of the field mirror. The light beam continues to diverge back to the twin mirrors and then focus again onto the field mirror, repeatedly. Finally, the beam exits the cell at the edge of the field mirror opposite to the point at which it was injected.

Every time the light beam reflects off the twin mirrors it encounters an effective aperture and diffracts. The diffraction (Fraunhofer) of a plane wave by a circular aperture may be expressed in terms of an Airy radius: (43)

$$r \approx 1.22 \frac{R\lambda}{D}$$

which is the radius of the diffraction pattern from the central maximum to the centre of the first dark ring, R is

the distance from the aperture, D is the aperture diameter, and λ is the wavelength.

As the beam reflects back and forth in the cell it might be expected that the beam spot on the field mirror would grow in size, as the result of successive diffractions. Conversely, it might be argued that the diffracted beam is refocussed to a spot on alternating twin mirror reflections. This argument relies on a Fourier optics analogue to the mirror system (43).

The light beam fills the twin mirror and diffracts, where the twin mirror can be considered the transform lens. The twin mirror converges the diffraction spot onto the field mirror. This is in the Fourier transform plane of the twin mirror and the Airy pattern formed is the two dimensional Fourier transform of the circular aperture. The diffraction spot now reflects to fill the other twin mirror, which can be considered the inverse transform lens. The inverse Fourier transform of the pattern at the field mirror (the Airy pattern) appears at the image plane of the inverse transform lens. Thus, the diffraction spot is reimaged to a point, and the beam is successively diffracted and reimaged every 4 transits of the cell.

To resolve this problem theoretically would be difficult, since rigorous diffraction calculations can be extremely complex. There is no formal treatment in the literature of a multiple pass system of this type. Born and Wolf (44) treat the related simpler problem of the

diffraction of a spherical wavefront by a circular aperture. The solution yields a diffraction pattern at the focal plane of the spherically converging beam that is the same as that for plane parallel wavefronts. However, the intensity of the central spot goes to zero on either side of the focal plane, along the optic axis. The distance along the optical axis between the null points of the central spot is called the focal tolerance. It is given by:

$$\Delta z \simeq \frac{1}{2}\left(\frac{f}{a}\right)^2 \lambda$$

where f is the focal length of the beam, 2a is the diameter of the aperture, and is the wavelength. In the White cell, the field mirror is in the focal plane of the twin mirror, therefore the diffraction spot on the field mirror should be the same as the Airy pattern. The focal tolerance for far-infrared light at 20 cm in this 1 meter cell is 10 cm. The drawing below from (44) shows the cross section of the intensity distribution of the diffraction pattern due to a circular aperture near the focus of a spherically converging light beam.

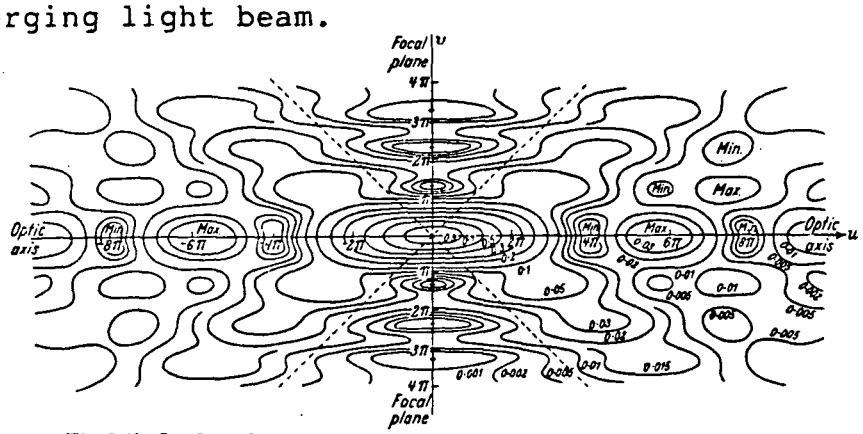

Fig. 8.41. Isophotes [contour lines of the intensity $I(u, v)$] in a meridional plane near focus of a converging spherical wave diffracted at a circular aperture. The intensity is normalized to unity at focus. The dotted lines represent the boundary of the geometrical shadow. When the figure is rotated about the u-axis, the minima on the v-axis generate the AIRY dark rings.

An experiment to measure the diffraction spot size on successive reflections in the mirror cell has been performed. The experiment's design is drawn schematically below.

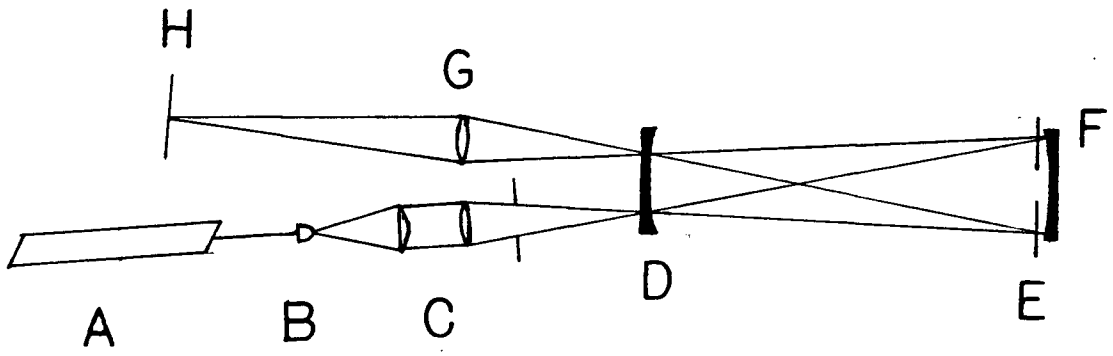

The HeNe laser A illuminates the microscope objective B to form a diverging beam. The lenses and iris combination C define a beam which focusses at the edge of the field mirror and fills the twin mirror F. A variable aperture or pinhole E is placed in front of the twin mirror. The beam exits the cell and the diffraction pattern is focussed by the lens G onto the screen H.

Radiation corresponding to path lengths of 2 , 6 , 10 , ... are transmitted by the cell used in this experiment, where is the length of the cell (this is different from the cell designed here). The aperture is placed only over one twin mirror. Therefore, light corresponding to a path length of 2 passes through the aperture once, 6 passes through twice, etc.

Using a 3 mm diameter aperture, the same Airy pattern

was observed on the screen for path lengths of 2, 6, 10, 14, 18, and 34ℓ, corresponding to 1, 2, 3, 4, 5, and 9, passes through the aperture. The Airy disk diameter measured on the screen, taking into account the magnification by the lens G, is the same as predicted by eqn. 4.1 to better than 10%. In addition, an experiment was conducted with an aperture diameter of 0.3 mm. Again, the same diffraction pattern is observed for pathlengths of 2, 6, 10ℓ. The measured Airy disk diameter was the same as the predicted diameter, where the error in the prediction and in the measurement is less than 10%.

These experiments demonstrate that the diffraction spot does not grow with successive reflections and that neither of the proposed arguments is correct. A more satisfactory explanation may lie in the fact that most of the light intensity of the diffracted beam lies in the central spot. The observation of the diffraction pattern from a single aperture even after repeated reflections may just be the most recent diffraction of the central spot. The outer rings of previous diffractions have little intensity and are obscured by the Airy pattern of the last diffraction. An indication of what is happening here might be found by making intensity measurements of the central spot on successive diffractions. It would be interesting and valuble to continue this investigation since no previous work, either experimental or theoretical, on the diffraction of light in a White cell has been found.

V. CONCLUSION

The present work covers aspects of collision induced absorption by homonuclear diatomic molecules. The prevalence of this species of molecules in the astrophysical environments of planetary atmospheres and galactic molecular clouds makes their far-infrared spectra particularly interesting. The simulation in the laboratory of conditions similar to these environments has been the major motivation for this work. The research reported here has involved: an investigation of the theory of collision induced absorption, a measurement of the far-infrared (5 - 70 cm^{-1}) absorption spectra of liquid nitrogen and liquid oxygen at 77K, and the design of a low temperature, long path length, optical absorption cell. The far-infrared spectrum of liquid oxygen measured here has not previously been published.

It is desirable to increase the spectral bandwidth of both the nitrogen and oxygen measurements to encompass the entire rotational band, and thereby obtain the integrated absorption coefficient. This could provide information on the molecular interactions within the liquid, if a suitable theory of these liquids existed. Good measurements of the entire rotational band of these molecules in the liquid phase might motivate the development of such a theory. In addition, a liquid nitrogen absorption spectrum extended to higher frequencies might help determine if liquid nitrogen is present on the surface of Neptune's moon Triton when the Voyager far-infrared spectra are examined.

Work on the far-infrared absorption by cold hydrogen gas, with the goal of observing dimer absorption, is continuing. The completion of the low temperature cell is expected in the near future and these experiments will begin shortly thereafter. Further investigation of diffraction within the cell optical system would be valuable, since this type of cell is frequently used in spectroscopy experiments and there is presently no discussion of this issue in the literature.

REFERENCES

1. G. E. Ewing, C. J. P. , 54, 487 (1976)

2. A. Watanabe, H. L. Welsh, C. J. P. ,43, 818 (1965)

3. A. R. W. McKellar, H. L. Welsh, C. J. P. , 52, 1082 (1974)

4. A. R. W. McKellar, C. J. P. , 62, 760, (1984)

5. L. Frommhold, R. Samuelson, G. Birnbaum, Ap. J. , 283, L79 (1984)

6. U. Fink, H. P. Larson, Ap. J. , 233, 1021 (1979)

7. E. F. Erickson et al, Icarus, 35, 61 (1978)

8. R. Hanel and the Voyager Infrared Spectrometer Team, Science 204, 972 (1979)

9. R. Hanel et al, Science, 206, 952 (1979)

10. R. Hanel et al, Science, 212, 192 (1981)

11. R. Hanel et al, Science, 215, 544 (1979)

12. R. Courtin, Icarus, 51, 466 (1982)

13. D. Morrison, Ann. Rev. Ast. Astro. , 20, 469 (1982)

14. D. P. Cruickshank, P. M. Silvaggio, Ap. J. , 233, 1016 (1979)

15. R. H. Brown, D. P. Cruickshank, Sci. Am. , 253, 38 (July 1985)

16. J. Van Kranendonk, Z. J. Kiss, C. J. P. , 37, 1187 (1959)

17. J. P. Colpa, J. A. A. Ketelaar, Mol. Phys. , 1, 343 (1958)

18. M. M. Shapiro, Ph. D. Thesis, University of Toronto, Toronto, Ontario (1965)

19. J. D. Poll, J. L. Hunt, C. J. P. , 59, 1448 (1981)

20. D. J. Griffiths, Introduction to Electrodynamics, Prentice-Hall, Englewood Cliffs, NJ (1981), pg. 130.

21. N. W. B. Stone et al, C. J. P. , 62, 338 (1984)

22. A. D. Buckingham, R. L. Disch, D. A. Dunmuir, J. Am. Chem. Soc. , 90, 3104 (1968)

23. G. Birnbaum, Intermolecular Spectroscopy and Dynamical Properties of Dense Systems, Edited by J. Van Kranendonk, North-Holland, Amsterdam, The Netherlands (1980), pg. 132.

24. G. Herzberg, Spectra of Diatomic Molecules, D. Van Nostrand, NY, NY (1950), pg. 107

25. A. I. P. Handbook, McGraw-Hill, NY, NY, pg. 7-168.

26. J. I. Steinfeld, Molecules and Radiation, MIT Press, Cambridge, Mass. (1981), pg. 107

27. H. P. Gush, Proceedings of 1983 Space Helium Dewar Conference, Edited by, J. B. Hendricks, G. R. Kerr, University of Alabama in Huntsville (1984), pg. 99.

28. M. Halpern, H. P. Gush, E. Wishnow, V. DeCosmo, submitted to Ap. Optics (1985)

29. M. Halpern, Ph. D. Thesis, MIT, Cambridge, Mass. (1983)

30. D. R. Bosomworth, H. P. Gush, C. J. P. , 43, 751 (1965)

31. U. Buontempo, S. Cunsolo, G. Jacucci, J. J. Weis, J. Chem. Phys. , 63, 2570 (1975)

32. I. R. Dagg et al, C. J. P. , 63, 625 (1985)

33. N. W. B. Stone, D. Williams, Mol. Phys. , 1, 85 (1965)

34. J. L. Urbaniak, I. R. Dagg, G. E. Reesor, C. J. P. , 55, 496 (1977)

35. M. M. Shapiro, H. P. Gush, C. J. P. , 44, 949 (1966)

36. C. R. C. Handbook, Chemical Rubber Co. , Cleveland, OH (1971), pg. E-43.

37. M. Evans, Mol. Phys. , 29, 1345 (1975)

38. S. Cunsolo, H. P. Gush, C. J. P. , 2058 (1972)

39. J. U. White, J. O. S. A. , 32, 285 (1942)

40. R. P. Blickensderfer, G. E. Ewing, R. Leonard, Ap. Optics, 7, 2214 (1968)

41. D. Horn, G. C. Pimental, Ap. Optics, 10, 1892 (1971)

42. G. K. White, Experimental Techniques in Low Temperature

Physics, Oxford, London, (1968). pg. 220.

43. E. Hecht, A. Zajac, Optics, Addison-Wesley, Reading, Mass. (1979)

44. M. Born, E. Wolf, Principles of Optics, Pergammon, London (1959) pg. 439.